

# Metrics of High Cofluctuation and Entropy to Describe Control of Cardiac Function in the Stellate Ganglion

Nil Z. Gurel<sup>1\*,†</sup>, Koustubh B. Sudarshan<sup>3,†</sup>, Joseph Hadaya<sup>1,2</sup>, Alex Karavos<sup>3</sup>, Taro Temma<sup>1</sup>, Yuichi Hori<sup>1</sup>, J. Andrew Armour<sup>1</sup>, Guy Kember<sup>3</sup>, Olujimi A. Ajijola<sup>1,2</sup>

\*For correspondence:  
gurelnil@gmail.com (FMS)

<sup>†</sup>These authors contributed  
equally to this work

<sup>1</sup> UCLA Cardiac Arrhythmia Center and UCLA Neurocardiology Research Program of Excellence, Los Angeles, CA; <sup>2</sup>UCLA Molecular, Cellular, and Integrative Physiology Program, Los Angeles, CA; <sup>3</sup>Department of Engineering Mathematics and Internetworking, Dalhousie University, Nova Scotia, Canada

**Abstract** Stellate ganglia within the intrathoracic cardiac control system receive and integrate central, peripheral, and cardiopulmonary information to produce postganglionic cardiac sympathetic inputs. Pathological anatomical and structural remodeling occurs within the neurons of the stellate ganglion (SG) in the setting of heart failure. A large proportion of SG neurons function as interneurons whose networking capabilities are largely unknown. Current therapies are limited to targeting sympathetic activity at the cardiac level or surgical interventions such as stellectomy, to treat heart failure. Future therapies that target the stellate ganglion will require understanding of their networking capabilities to modify any pathological remodeling. We observe SG networking by examining cofluctuation and specificity of SG networked activity to cardiac cycle phases. We investigate network processing of cardiopulmonary transduction by SG neuronal populations in porcine with chronic pacing-induced heart failure and control subjects during extended in-vivo extracellular microelectrode recordings. We find that information processing and cardiac control in chronic heart failure by the SG, relative to controls, exhibits: i) more frequent, short-lived, high magnitude cofluctuations, ii) greater variation in neural specificity to cardiac cycles, and iii) neural network activity and cardiac control linkage that depends on disease state and cofluctuation magnitude.

## Introduction

Neural control of cardiac function involves adaptive adjustment of mechanical and electrical activity to meet the organism's demand for blood flow. This cardioneural control scheme consists of neural populations in the central, peripheral, and intrinsic cardiac nervous systems. Interactions among components of the cardiac nervous system highlight that these neural populations work in concert, rather than as independent, singular processing units (*Ardell et al., 2016*). From an information processing standpoint, the operation of these interconnected neural networks has evolved to coordinate cardiac function on a beat-by-beat basis, producing the "functional" outputs of this control scheme such as blood pressure, heart rate, or respiratory pressure and rate. Localized adaptations in the cardioneural network in response to pathology can cause an evolution of global network properties with heightened risk of poor outcomes without measurable evidence

40 from these functional outputs (Deyell et al., 2015; Kember et al., 2013).

41 There is a current focus on understanding cardioneural network processing within the stel-  
42 late ganglion (SG), a collection of nerves serving as the major source of sympathetic input to the  
43 heart (Mehra et al., 2022). The SG (located in either side of the neck) operates as an integrative  
44 layer within the control hierarchy where it processes central cardiac inputs to the heart, receives  
45 cardiac feedback, and projects efferent control outputs to the heart. In pathological states such as  
46 heart failure (HF), morphological and neurochemical remodeling of SG neurons has been reported  
47 in both animal models (Ajijola et al., 2013; Han et al., 2012; Ajijola et al., 2015; Nakamura et al.,  
48 2016) and in humans (Ajijola et al., 2020, 2012b). Due to its key role in proarrhythmic neural signal-  
49 ing and convenience in surgical accessibility, clinical interventions targeting SG are used to treat  
50 various cardiovascular conditions (Vaseghi et al., 2012, 2017; Ajijola et al., 2012a). It has also been  
51 established that an enhanced cardiac sympathetic afferent reflex contributes to sympathoexcita-  
52 tion and pathogenesis of heart failure (Wang and Zucker, 1996; Ma et al., 1997; Chen et al., 2015;  
53 Wang et al., 2017, 2008, 2014; Gao et al., 2005, 2007). Despite these novel interventions and gen-  
54 eral understanding, SG clinical therapy will remain largely unexplored without greatly improved  
55 understanding of SG neuronal information processing in healthy versus pathological states. Prior  
56 studies examining the SG neural activity have been limited to in vivo extracellular recordings (Ar-  
57 mour, 1983, 1986; Armour et al., 1998; Yoshie et al., 2020, 2018).

58 Recently, we explored network processing of cardiopulmonary transduction by SG neuronal  
59 populations in healthy porcine, defining a novel metric 'neural specificity' that measures specificity  
60 of neural firing patterns to cardiopulmonary signals (Sudarshan et al., 2021). This metric is con-  
61 trastive and a measure of the difference between the probability density function (PDF) of neural  
62 'sampling' of a control target relative to the same in the random sampling limit. While the target,  
63 left ventricular pressure (LVP) considered here is periodic this is not a necessary condition for use  
64 of the specificity metric; it is also applicable to aperiodic signals in an event-based fashion.

65 In the current work, we investigate differences in information transfer between control and  
66 heart failure porcine models with multi-channel electrode arrays. We first uncover network-level  
67 spatiotemporal dynamic signatures by quantifying short-lived high co fluctuation events in neural  
68 activity. Second, we study coherence and consistency in the evolution of neural specificity with re-  
69 spect to the control target. Third, we expose differences in neural specificity and its coherence and  
70 consistency, via entropy, inside and outside co fluctuation events. These differences are consid-  
71 ered for control and heart failure models and quantify differences in the maintenance of function  
72 between these groups.

## 73 Results

74 Neural activity was measured over 16 channels along with simultaneous left ventricular pressure  
75 (LVP) for approximately six hours of continuous recordings per animal. Representative neural ac-  
76 tivity recording for a single channel, LVP, and representative spike trains are displayed for control  
77 and heart failure animals in Fig. 6A. A total of 17 Yorkshires (6 control, 11 HF, Fig. 6D) underwent  
78 the terminal experiment described in Fig. 6E. Upon the signal processing pipeline described above,  
79 we computed two event rate measures per animal as the final product representing the co fluctu-  
80 ations ( $ER_{MEAN}$ ,  $ER_{STD}$ ). As the metric representing the neural specificity, we computed two en-  
81 tropy measures per channel ( $Entropy_{MEAN}$ ,  $Entropy_{STD}$ ), resulting in a total of sixteen  $Entropy_{MEAN}$   
82 and sixteen  $Entropy_{STD}$  per animal. Finally, we used these metrics to quantify: i) neural popu-  
83 lation dynamics (i.e.,  $ER_{MEAN}$ ,  $ER_{STD}$ ), ii) neural specificity to target LVP, or cardiac control (i.e.,  
84  $Entropy_{MEAN}$ ,  $Entropy_{STD}$ ), and iii) Linkage between neural population dynamics and specificity (i.e.,  
85  $Entropy_{MEAN,EVENT}$ ,  $Entropy_{STD,EVENT}$ ).

## 86 Stellate Ganglion in Heart Failure Exhibits High Event Rate

87 Fig. 1A-B show event rate outcomes grouped by heart failure (HF) models and controls. HF animals  
88 show significantly higher event rates compared to control animals for both  $ER_{MEAN}$  ( $p = 0.011$ ,

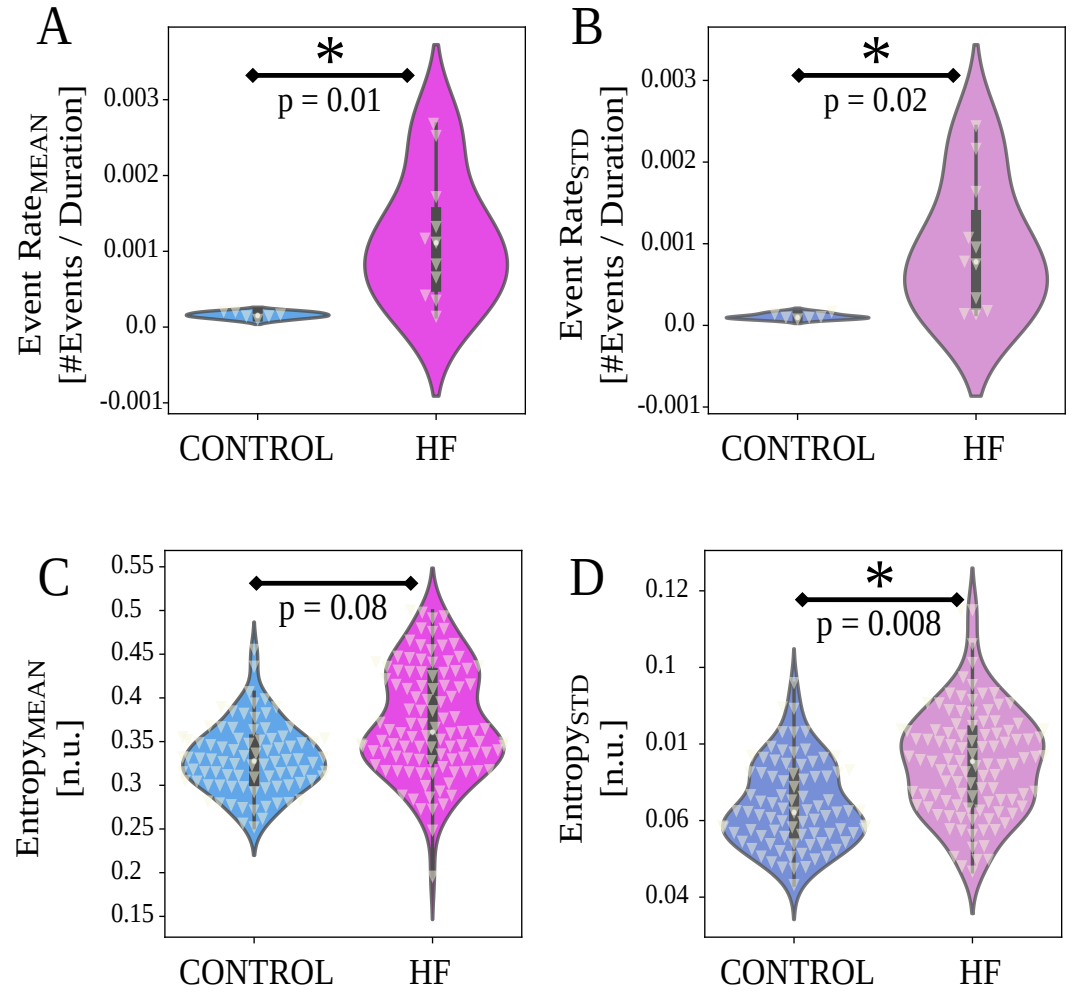


**Figure 1.** Event rate ( $ER$ ) and entropy results between control and HF animals (horizontal axes). White triangles indicate data points. A-B) Heart failure (HF) group animals show higher  $ER_{MEAN}$  and  $ER_{STD}$  compared to control group ( $p < 0.05$ ). C-D) HF group animals show higher entropy variability ( $Entropy_{STD}$ , Eq. (2),  $p = 0.008$ , in D), and no difference in  $Entropy_{MEAN}$  (Eq. (2),  $p = 0.08$ , in C). For  $ER$ , p-values are from two-sample t-test or Wilcoxon rank-sum tests, depending on normality. For entropy, p-values are from linear mixed effects (LME, Eq. (2)) detailed in Methods.

89 effect size  $d = 1.59$ ,  $ER_{MEAN,HF} = 0.0012 \text{ evts/sec}$ ,  $ER_{MEAN,Controls} = 0.0002 \text{ evts/sec}$  ) and  $ER_{STD}$  ( $p =$   
90  $0.023$ ,  $d = 1.48$ ,  $ER_{STD,HF} = 0.001 \text{ evts/sec}$ ,  $ER_{STD,Controls} = 0.0001 \text{ evts/sec}$ ). The cofluctuation time  
91 series for each animal is depicted in Fig. 3, where the event time series are computed. The ‘events’  
92 or short-lived intervals where high cofluctuations exist are shown as level 1, leading to the event  
93 time series in Fig. 4. We observe that the cofluctuations are more localized in HF animals with  
94 greater heterogeneity.

### 95 HF Animal Models Have Heavy Tailed Cofluctuation Distributions

96 We qualitatively explored the statistical distribution of the cofluctuation time series. Fig. 2 shows  
97 log-normal fits for each animal group for  $Cofluctuation_{MEAN}$  and  $Cofluctuation_{STD}$  time series, along  
98 with 68% confidence interval (CI) bounds, mean of fit ( $\mu_{FIT}$ ) and standard deviation of fit ( $\sigma_{FIT}$ ).  
99 Control animals (Fig. 2A-B) exhibit narrow confidence intervals, lower ( $\mu_{FIT}$ ) and ( $\sigma_{FIT}$ ) values, and  
100 tighter log-normal fits. In contrast, HF animals (Fig. 2C-D) exhibit wider confidence intervals, higher  
101 ( $\mu_{FIT}$ ) and ( $\sigma_{FIT}$ ) values, and poorer log-normal fits. Of note, HF animals have heavy tails ranging  
102 further outside of confidence bounds.

### 103 Stellate Ganglion Shows Greater Variation in Neural Specificity to LVP in Heart Fail- 104 ure

105 We next examined the neural specificity to LVP, quantified by entropy measures in Eq. (2). Fig.  
106 1C-D shows  $Entropy_{MEAN}$  and  $Entropy_{STD}$ , grouped by animals. Compared to the control group,  
107 stellate ganglion of HF animals exhibited significantly higher  $Entropy_{STD}$  (variation in entropy, Fig.  
108 1D, adjusted  $\beta = 0.01$  n.u., 95%  $CI = \pm 0.01$  n.u.,  $d_{RM} = 0.73$ ,  $p = 0.009$ ). However, there is no  
109 significant difference in  $Entropy_{MEAN}$  (mean entropy) between animal groups. (Fig. 1C,  $\beta = 0.04$   
110 n.u.,  $\pm 0.05$  n.u.,  $d_{RM} = 0.82$ ,  $p = 0.087$ ).

### 111 Neural Network Activity and Cardiac Control Linkage Depends on Animal Group 112 and Cofluctuation Magnitude

113 We explored the nature of cardiac control inside and outside short duration regions of high cofluc-  
114 tuation, i.e. ‘events’, characterized by strongly coherent stellate neural activity patterns. Insight  
115 into how these events may be relevant to cardiac control is considered here in the context of how  
116 control differs inside and outside events and termed ‘event entropy’.

117 First, we studied the extent to which event entropy differs inside and outside of events (Fig. 5A,  
118 C, event type as fixed effect in Eq. (9)). Second, we studied whether event entropy is sensitive to  
119 the animal type characterized here as control or HF (Fig. 5B, D, animal type as fixed effect in Eq.  
120 (9)).

121 Regardless of the animal group,  $Entropy_{MEAN, NON-EVENT}$  significantly exceeds  $Entropy_{MEAN, EVENT}$   
122 (Fig. 5A,  $\beta = 0.007$  n.u.,  $\pm 0.004$  n.u.,  $d_{RM} = 0.07$ ,  $p < 0.001$ ). Similarly,  $Entropy_{STD, NON-EVENT}$  signif-  
123 icantly exceeds  $Entropy_{STD, EVENT}$  (Fig. 5C,  $\beta = 0.01$  n.u.,  $\pm 0.002$  n.u.,  $d_{RM} = 0.29$ ,  $p < 0.001$ ). An  
124 examination of the contribution of each animal group showed no significant difference between  
125 groups for  $Entropy_{MEAN, EVENT}$  (Fig. 5B,  $\beta = 0.06$  n.u.,  $\pm 0.05$  n.u.,  $d_{RM} = 1.13$ ,  $p = 0.07$ ). On the other  
126 hand, HF animals exhibited an increase in  $Entropy_{STD, EVENT}$  compared to control animals (Fig. 5D,  
127  $\beta = 0.02$  n.u.,  $\pm 0.02$  n.u.,  $d_{RM} = 0.75$ ,  $p = 0.012$ ). These analyses imply that the linkage between  
128 neural network function and cardiac control differs inside and outside of cofluctuation events and  
129 between animal groups in the stellate ganglion.

### 130 Discussion

131 In this work, we performed a novel investigation of SG neural population dynamics and neural  
132 specificity to continuous left ventricular pressure in control and heart failure Yorkshire pigs. The  
133 methods in this work are intended to measure the way population neural activity relates to closed-  
134 loop control of a target and how that computation changes in diseased states. This was applied  
135 here to closed-loop control of cardiac output where the assumed target was LVP.



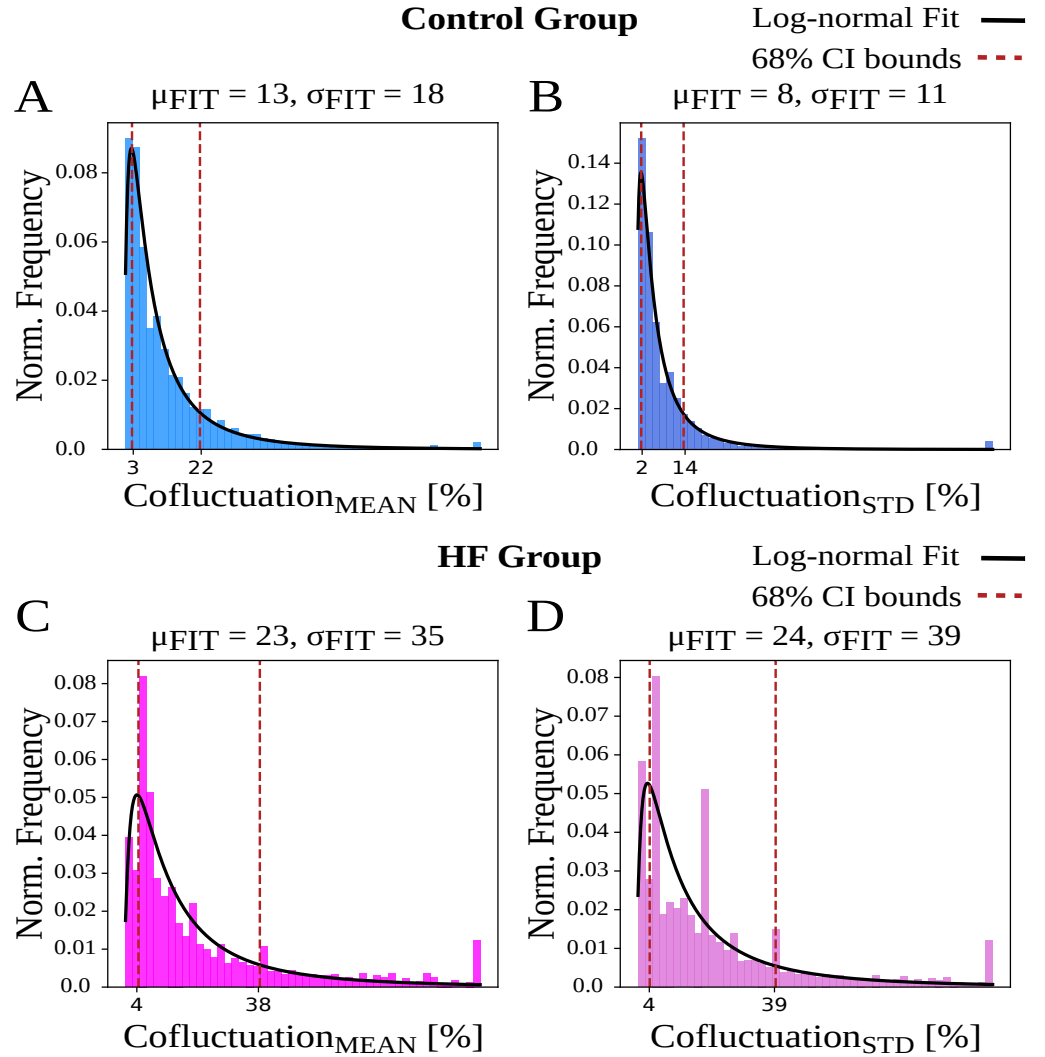


**Figure 2.** Cofluctuation histograms (calculated from mean or standard deviation of sliding spike rate, referred as  $Cofluctuation_{MEAN}$  and  $Cofluctuation_{STD}$ , respectively) and log-normal fits for each animal group.  $\mu_{FIT}$  and  $\sigma_{FIT}$  are the respective mean and standard deviation (STD) of fitted distribution, used for 68% confidence interval bounds. A-B) Control animals have narrower bounds and represent a better fit to log-normal distribution. C-D) Heart failure (HF) animals display more heavily skewed distributions that indicate heavy tails.

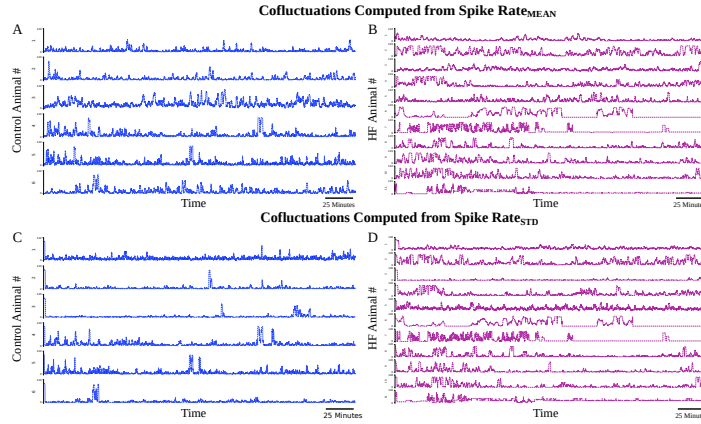


**Figure 3.** Cofluctuations time series at convergent  $C$  values for each animal. A) Cofluctuations from coactivity calculation from mean of sliding spike rate for control animals. B) Cofluctuations from coactivity calculation from mean of sliding spike rate for HF animals. C) Cofluctuations from coactivity calculation from standard deviation of sliding spike rate for control animals. D) Cofluctuations from coactivity calculation from standard deviation of sliding spike rate for HF animals.

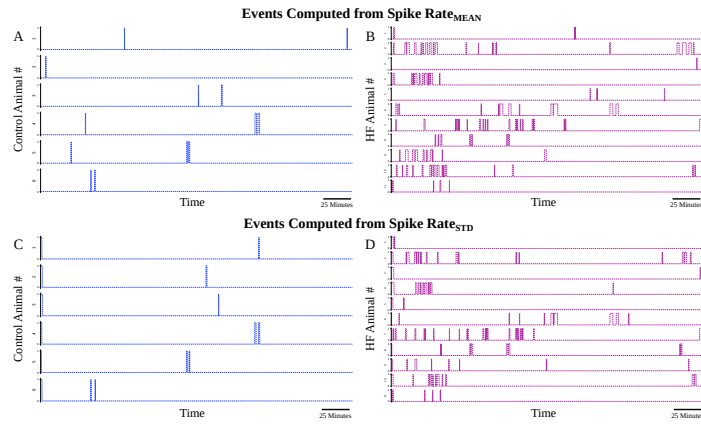


**Figure 4.** Events time series at convergent  $(C, T)$  pairs for each animal. A) Events from coactivity calculation from mean of sliding spike rate for control animals. B) Events from coactivity calculation from mean of sliding spike rate for HF animals. C) Events from coactivity calculation from standard deviation of sliding spike rate for control animals. D) Events from coactivity calculation from standard deviation of sliding spike rate for HF animals.

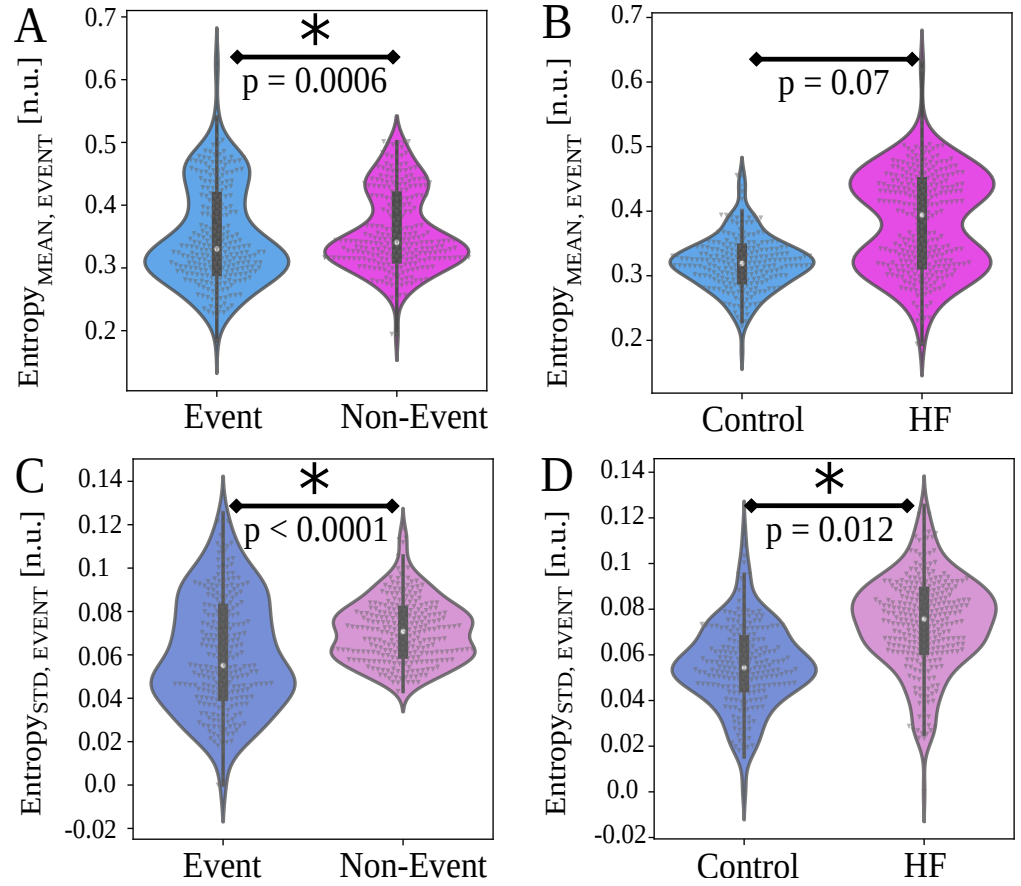


**Figure 5.** Event entropy Eq. (2) investigation involved consideration of entropy values inside and outside of event regions. A) There is significant difference between in  $Entropy_{MEAN, EVENT}$  and  $Entropy_{STD, EVENT}$  across all animals ( $p = 0.0006$ ). B) There is no significant difference in  $Entropy_{MEAN, EVENT}$  between animal groups ( $p = 0.07$ ). C) There is significant difference in  $Entropy_{STD, EVENT}$  between events and non-events across all animals ( $p < 0.0001$ ). D) There is significant difference in  $Entropy_{STD, EVENT}$  between animal groups ( $p < 0.012$ ).

136 The methods in this work involved

- 137 • *Neural Specificity* A measure of bias in neural activity toward ‘sampling’ of specific target states.  
138 The target specificity is a contrastive measure that compares neural sampling of a target  
139 relative to random sampling of the same target.
- 140 • *Neural Specificity Coherence* Entropy of neural specificity was used to measure coherence of  
141 neural specificity as a function of time.
- 142 • *Cofluctuation Events* The degree of coactivity in the dynamics of the mean and its standard  
143 deviation was measured between pairs of channels from minimum to maximum physical  
144 separation and this exposed short duration ‘events’ when cofluctuation was unusually high.
- 145 • *Event Entropy* Functional significance of cofluctuation events was evaluated by comparing dif-  
146 ferences in the degree of neural specificity coherence inside and outside of events.

## 147 **Prevalence of Short-Lived Cofluctuations in SG Activity in HF**

148 In prior work, we identified neural specificity toward near-peak systole of the LVP waveform in con-  
149 trol animals (*Sudarshan et al., 2021*). Application of this metric and the construction of a related  
150 coherence measure provided insight into differences in neural processing dynamics between con-  
151 trol and HF animals. Our results show that cardiac control exerted within diseased states has  
152 greater variation in entropy and thus less consistency for heart failure animals compared to con-  
153 trol animals. This finding may extend to other pathologies for which the cardiac control hierarchy  
154 is disrupted.

## 155 **Neural Network Activity is Linked to Cardiac Control**

156 Based on the effect size ( $d_{RM}$ ), event entropy magnitude appears to be higher with greater variation  
157 observed in HF animals compared to control animals (Fig. 5B-D). This implies a level of increased  
158 unpredictability and increased difficulty in cardiac control for animals in heart failure over control  
159 animals.

160 A limitation of this result is that the effect sizes for event versus non-event comparisons are  
161 small to medium, which potentially indicates a larger study is necessary to better understand the  
162 physiological contributions from event type. Another limitation of the study lies in the absence  
163 of multiple-class pathologies (i.e., different heart failure models or other reproducible models)  
164 and in the absence of stratified pathologies (i.e., animal models with varying degrees of heart fail-  
165 ure). Measurement of these neurocardiac metrics during slow, quasi-static application of clinically-  
166 relevant stressors (*Akeju and Brown, 2017; Chamadia et al., 2019*) should provide unique opportu-  
167 nities to investigate unresolved questions. Future studies should focus on expanding the dataset  
168 to examine how these metrics change with varying pathologies or varying disease models. We also  
169 cannot exclude possible effects of general anesthesia, open chest and open pericardial effects on  
170 our findings, though the effects are likely consistent across the groups studied in the same manner.

## 171 **Conclusion**

172 In this study, we looked, for the first time to our knowledge, at long-term studies of in vivo car-  
173 diac control in baseline states. The baseline states provide unique signatures that differentiate  
174 animals with heart failure and controls. We discovered the inputs (i.e., neural signals) and outputs  
175 (i.e., blood pressure) are linked, which led us to develop metrics to analyze the dynamical state of  
176 this networked control (*Gurel et al., 2022*). The primary observation has been that event-based  
177 processing within the stellate ganglion and its relationship to cardiac control is strongly modified  
178 by heart failure pathology. Our analysis is pointing to heart failure being best considered as a  
179 spectrum rather than a binary state. The magnitude of cofluctuation and neural specificity may  
180 give us a measure of the degree of heart failure and insight the extent to which cardiac control is  
181 compromised with respect to neural specificity and/or cofluctuation. Future therapies may bene-  
182 fit from being able to infer the degree of heart failure in terms neural markers as represented in

this work, in a less invasive way. Intriguing connections involve the alignment of our work with a growing consensus in neuroscience. Spatiotemporal changes in neural activity and linkages with control targets are associated with behavioral changes and the onset and development of specific pathologies. For instance, spatiotemporal brain-wide cofluctuations were reported to reveal major depression vulnerability (Hultman et al., 2018). Neural ensembles were linked to visual stimuli in mice Miller et al. (2014). Another study reported that brain's functional connectivity is driven by high-amplitude cofluctuations and that these cofluctuations encode subject-specific information during experimental tasks (Esfahlani et al., 2020). Similar cofluctuations were also reported to inform olivary network dynamics in the form of state changes in learning new motor patterns in mice (Wagner et al., 2021). Unique co-activation patterns in spontaneous brain activity indicated a signature for conscious states in mice (Gutierrez-Barragan et al., 2022). Global brain activity has also been linked to higher level social behaviours (Mague et al., 2022). These parallel conclusions in cardiac and neuroscience studies indicate similar experimental methods used to measure neural integration relative to control targets. Such measurements may be instrumental to design and assess the efficacy of neurally-based clinical interventions both at the level of the brain and the stellate ganglion.

## Methods

### Animal Experiments

Fig. 6 presents the conceptual overview and study design. The study was performed under a protocol approved by the University of California Los Angeles (UCLA) Animal Research Committee (ARC), in compliance with the UCLA Institutional Animal Care and Use Committee (IACUC) guidelines and the National Institutes of Health (NIH) Guide for the Care and Use of Laboratory Animals (Protocol: ARC 2015-022). Fig. 6D-E summarizes the studied animal groups and experimental pipeline. Male Yorkshire pigs ( $n = 17$ ) weighing  $57.5 \pm 12\text{kg}$  ( $\text{mean} \pm \text{SD}$ ) were studied as control ( $n = 6$ ) and HF model ( $n = 11$ ) groups. For SG neural data collection, the animals were sedated with tiletamine and zolazepam (Telazol, 4-8mg/kg) intramuscularly, intubated, and maintained under general anesthesia with inhaled isoflurane (2%). Continuous intravenous saline ( $8-10\text{ml/kg/h}$ ) was infused throughout the protocol and animals were temperature maintained using heated water blankets ( $37^\circ\text{C} - 38^\circ\text{C}$ ).

Median sternotomy by an incision down the midline of the entire sternum was performed to have a wide view of the thoracic region (Fig. 6A). The pericardium was opened to expose the heart and both stellate ganglia. After surgical procedures, animals were transitioned to alpha-chloralose anesthesia ( $6.25\text{mg}/125\text{mL}$ ;  $1\text{mL/kg}$  for bolus,  $20 - 35\text{mL/kg}$  or titrated to effect for maintenance) with supplemental oxygen ( $2\text{L/minute}$ ) for in vivo neural recordings from the left stellate ganglion. The left carotid artery was exposed, and a pressure catheter (SPR350, Millar Inc., Houston, TX) was inserted to continuously monitor left ventricular pressure (LVP). Additionally, three-lead surface electrocardiogram (ECG) and respiratory pressure (RP) were monitored continuously, and sampled at  $1\text{kHz}$ . Arterial blood gas contents were monitored at least hourly to ensure appropriate experimental conditions. At the end of the protocol, animals were euthanized under deep sedation of isoflurane and cardiac fibrillation was induced.

The heart failure model was created with implanted pacemakers (Viva Cardiac Resynchronization Therapy-Pacemaker, Biotronik, Lake Oswego, OR), as previously described (Hori et al., 2021), and summarized in Fig. 6D. After implantation, animals had a recovery period of 48 hours and chronic bigeminy pacing was initiated from the right ventricle. This process produces premature ventricular contractions (PVCs) which lead to cardiomyopathy, also known as PVC-induced cardiomyopathy (Blaye-Felice et al., 2016). To confirm the progression of cardiomyopathy, echocardiography was performed, before and after implantation. After the animals have been confirmed to have cardiomyopathy (referred as HF animals) at eight weeks after implantation, surgical procedures described in Fig. 6E were performed, and extracellular recordings were obtained from the left stellate ganglion, shown in Fig. 6A. It should be noted that a subset of HF animals ( $n = 6$ )

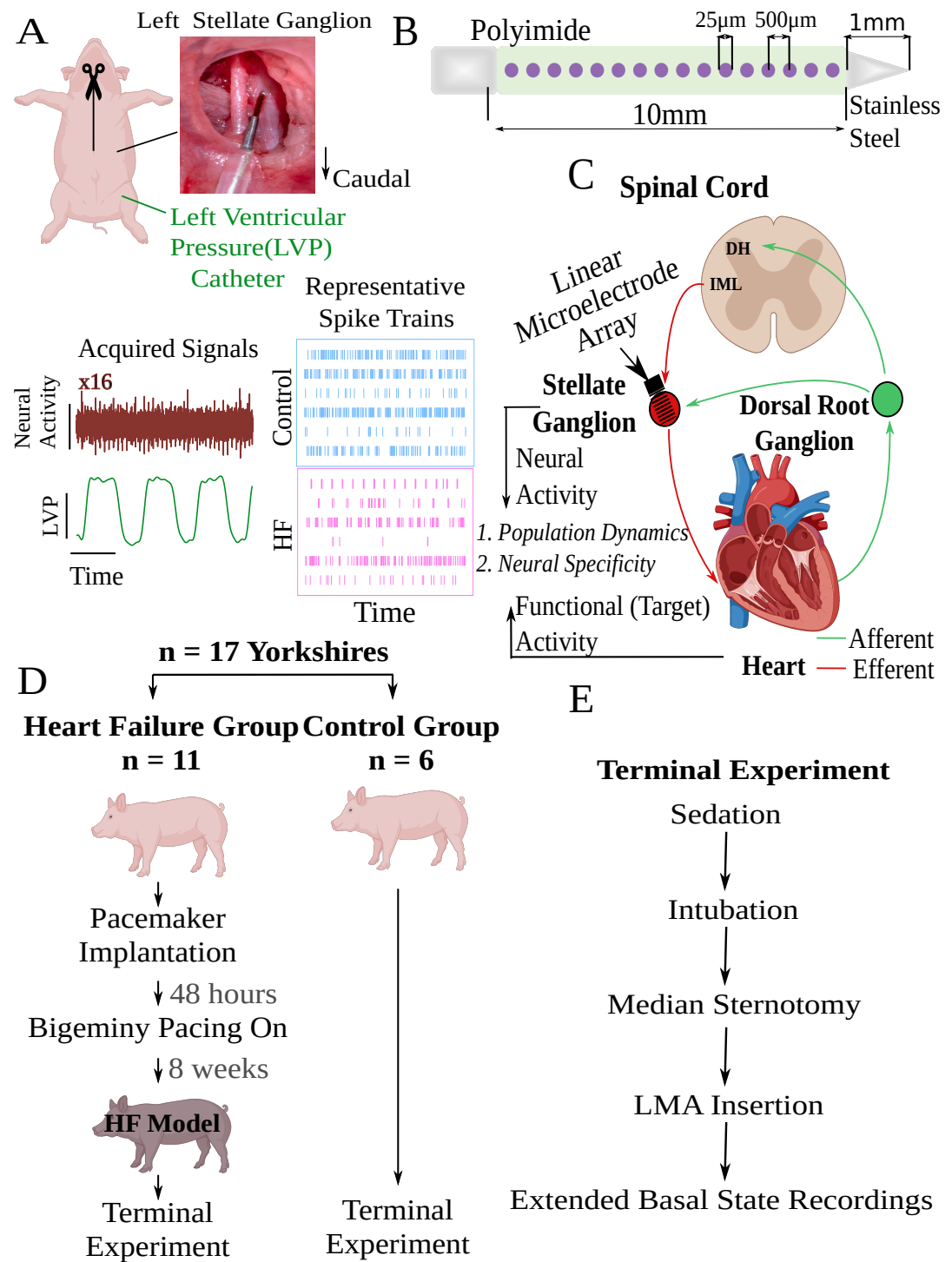


**Figure 6.** Experimental workflow and overall concept. A) A linear microelectrode array (LMA) was inserted to the left stellate ganglion (SG) for each animal. A total of 16 channels of neural activity were collected along with simultaneous left ventricular pressure (LVP). Representative spike trains are displayed for each animal group. B) Specifications of the LMA. C) Conceptual representation of this work. SG receives efferent and afferent information from the spinal cord's intermediolateral complex (IML) and dorsal root ganglion, respectively, and transmits efferent information to the heart. In this work, we investigate neural activity and its relationship to cardiac function as represented by a control target such as LVP. D) Among 17 Yorkshire pigs, 11 had heart failure induced by ventricular pacing, and 6 were in control group. SG recordings were collected at terminal experiments for both groups. E) Experimental flow describing the surgical preparation for the recordings. DH: Dorsal horn.

underwent an intervention, epicardial application of resiniferatoxin (RTX) to study its effects on the progression of cardiomyopathy as a separate study. However no significant effect of RTX was noted in any of the echocardiographic, serum, physiological, and autonomic tests (Hori et al., 2021). Hence, in this work, we combined RTX-treated HF animals with untreated HF animals.

We confirmed the RTX depleted the afferents by analyzing both structural and functional data (Hori et al., 2021). Structural depletion was proven with immunohistochemistry studies of the left ventricle (LV) and T1 dorsal root ganglion (DRG). Calcitonin gene-related peptide (CGRP)-immunoreactive fibers, a marker of sensory afferent nerves, was significantly reduced within the nerve bundles located in the LV for the RTX-treated group. Furthermore, the depletion of cardiac transient receptor potential vanilloid-1 (TRPV1) afferents was confirmed by the significant reduction of CGRP-expressing neurons in DRG. Functional depletion was proven by the response to the agonist of TRPV1 channel bradykinin and capsaicin. The RTX-treated group had a significantly lower LV pressure (LVP) response in the application of bradykinin and capsaicin, indicating that elimination of cardiac sympathetic afferent reflex was accomplished by RTX application in each case.

## SG Neural Recordings and Experimental Protocol

For each animal, a 16-channel, linear, single shank microelectrode array (LMA, Microprobes, Gaithersburg, MD) was inserted in the craniomedial pole of the left stellate ganglion (Fig. 6A). The LMA consisted of a polyimide tube of 0mm that contains recording sites, and a stainless steel tip of 1mm (Fig. 6B). Polyimide tube hosted a total of 16 platinum-iridium recording sites with 25μm radius, separated by 500μm intra-electrode spacing. A microelectrode amplifier (Model 3600, A-M Systems, Carlsborg, WA) was used to amplify (gain of 1000 – 2500) and filter (300Hz – 3kHz band-pass filter) the acquired signals. The signals were transferred to a data acquisition platform (Power 1401, Cambridge Electronic Design, Cambridge, UK) and recorded using Spike2 software (Cambridge Electronic Design, Cambridge, UK). All data were processed in Python and MATLAB. Increases in spike rate occur within 90-minutes of electrode insertion, hence a stabilization time of approximately three hours is required after the insertion takes place (Sudarshan et al., 2021).

It should be noted that our study deals with multi-electrode recordings of the closest neural populations to the electrode array. The earliest fundamental studies probing into cardiac nervous system used single-unit recordings, for which the target neurons should be isolated and appropriate low-impedance conductors should be used for obtaining high quality neural signals. Unlike these early studies, we used multi-unit (16-channel) electrode arrays to monitor the ensemble behaviors of SG neural populations. This experimental shift from single-unit to multi-unit recording has gained interest in the recent years in neurocardiology and neuroscience communities, offering an experimental view to the ensemble behaviors of neural populations (Gurel et al., 2022).

## Data Availability

Data is available in the Dryad repository  
<https://datadryad.org/stash/share/nEzGj21D1bUvrBYEtSNATZSAYTW39cBjjmV5RuVvleY>

## Signal Processing and Time Series Analysis

### Signal Processing Pipeline

A high-level description of the signal processing pipeline is in Fig. 7. In summary, Pearson's cross correlation is used to construct the coactivity matrix as the collection of cross correlations between all possible channel pairs. The coactivity matrix is computed at each timestamp and associated with a window of past neural activity (Fig. 7, 'Coactivity' block). This computation yields a causal sliding window of coactivity matrices referred to as the 'coactivity time series'.

Discrete events of high coactivity occurring in the coactivity time series are defined using two thresholds: (i) the coactivity time series is mapped to a univariate 'coactivity time series' where, at each timestamp, the percentage of coactivity matrix members exceeding a threshold  $C$  is



found, and (ii) discrete ‘events’ are defined as those timestamps when up-crossings of the cofluctuation time series through a second threshold  $T$  occur. The method used to choose the  $(C, T)$  pair, detailed in this section, generates discrete event timestamps and allows for the computation of the event rate ( $ER$ ) mean and standard deviation ( $STD$ ) statistics, which are used later in the statistical analyses. These cofluctuation events are regions that expose shifts in neural processing within the SG. These events are linked to function through the consideration of how neural specificity differs inside and outside cofluctuation events in control and heart failure animals.

The relationship between a control target such as LVP and neural activity at each channel is quantified via a continuously varying neural specificity (Sudarshan et al., 2021) (Fig. 7, ‘Neural Specificity’ block). The neural specificity is contrastive since it is the difference between the PDF of neural sampling of a target and the same found from random sampling. The neural activity in the SG is known to be a mixture of afferent, efferent, and local circuit activity derived from local circuit neurons with inputs from multiple sources. It in this sense that we define neural computation; when we observe the specificity to the target operating above or below the random sampling limit. Neural specificity is a multivariate signal measured across multiple target states at each channel as a function of time. This is reduced, for each channel, to a univariate time series by constructing its coherence in terms of entropy. The evolution of coherence in time provides access to the dynamics or consistency of neural computation. Detailed information about each signal processing step is provided in this section. Appendix 1 contains material detailing the mathematical aspects of the analysis. As stated in the signal processing block diagram, our outcome measures are event rate, entropy, event entropy. These metrics are developed in the Appendix 1.

### Unsupervised Spike Detection

We use a competitive, adaptive threshold, unsupervised approach for neural spike detection (Sudarshan et al., 2021). The algorithm initializes plus and minus barriers at the plus or minus signal maximum amplitude. The barriers are respectively lowered or raised until the plus or minus barrier ‘wins the competition’ and is the first to yield a minimal number of crossings. Detected spike regions are masked as a zero signal and the process repeated with barrier sizes further reduced in subsequent iterations. The competition is halted when one barrier is first to reach a minimal barrier height.

### Code Availability

Supporting Apache License codes are at GitHub (<https://github.com/Koustubh2111/Cofluctuation-and-Entropy-Code-Data>).

## Dataset and Statistical Analysis

Statistical analyses are performed in MATLAB Statistics & Machine Learning Toolbox (version R2021a) and Python SciPy Library (version 3.8.5).

### Sample Size Breakdown

Two channels were excluded from two animals due to insufficient signal quality. Within event rate analyses, all animals had sufficient neural data ( $n = 17$  animals, 6 control, 11 HF). Entropy analyses for 3 HF animals were excluded due to insufficient LVP quality resulting in  $n = 14$  animals (6 control, 8 HF).

### Outcome Measures

Within the signal processing pipeline described in Fig. 8, the event rate measures,  $ER_{MEAN}$  and  $ER_{STD}$ , are used to summarize the cofluctuation time series for each animal. A mean and standard deviation of the 16 channel-wise entropy time series results in 32 measures of entropy per animal (16 for  $Entropy_{MEAN}$  and 16 for  $Entropy_{STD}$  per animal).

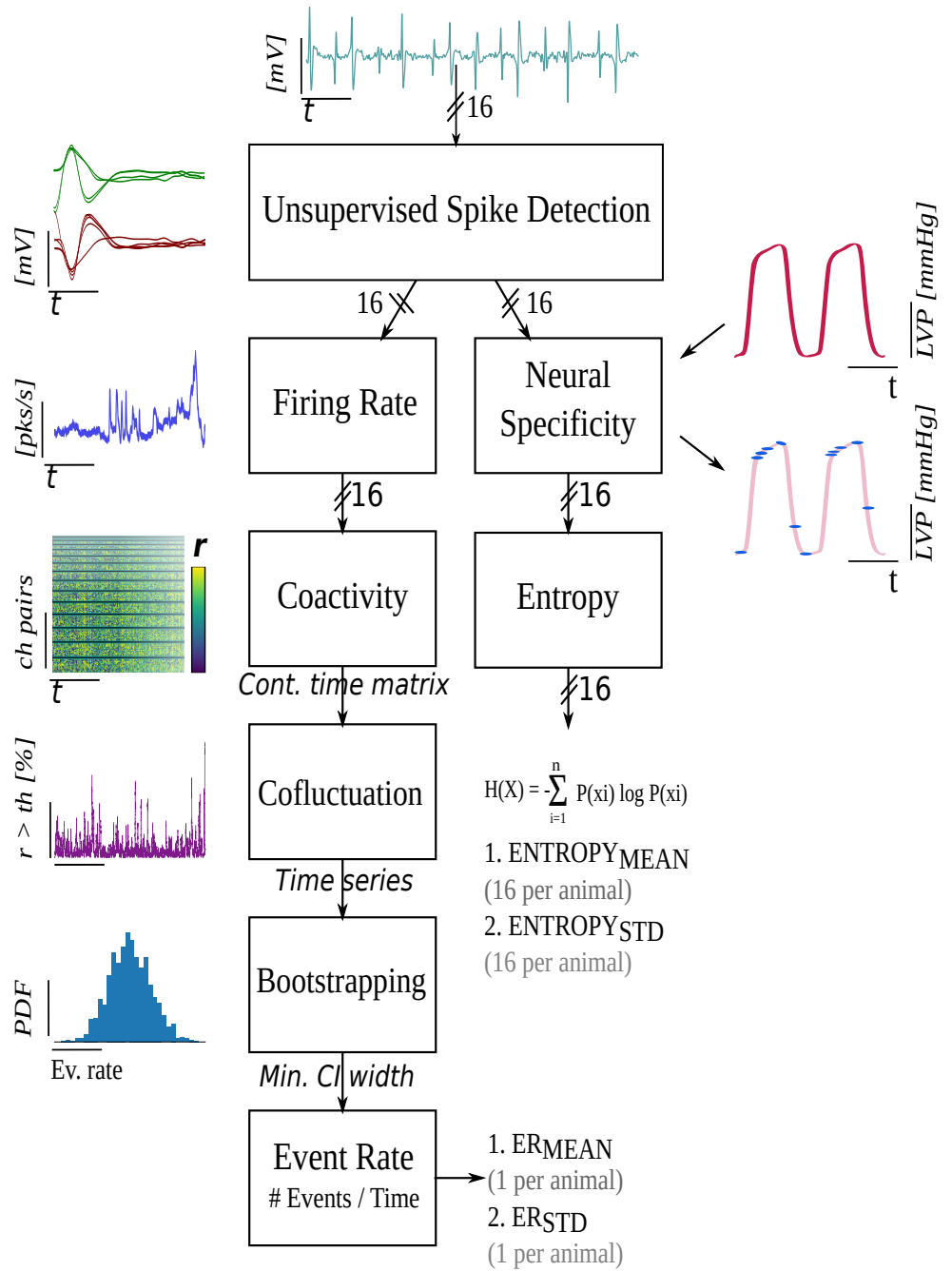


**Figure 7.** Signal Processing Block Diagram.

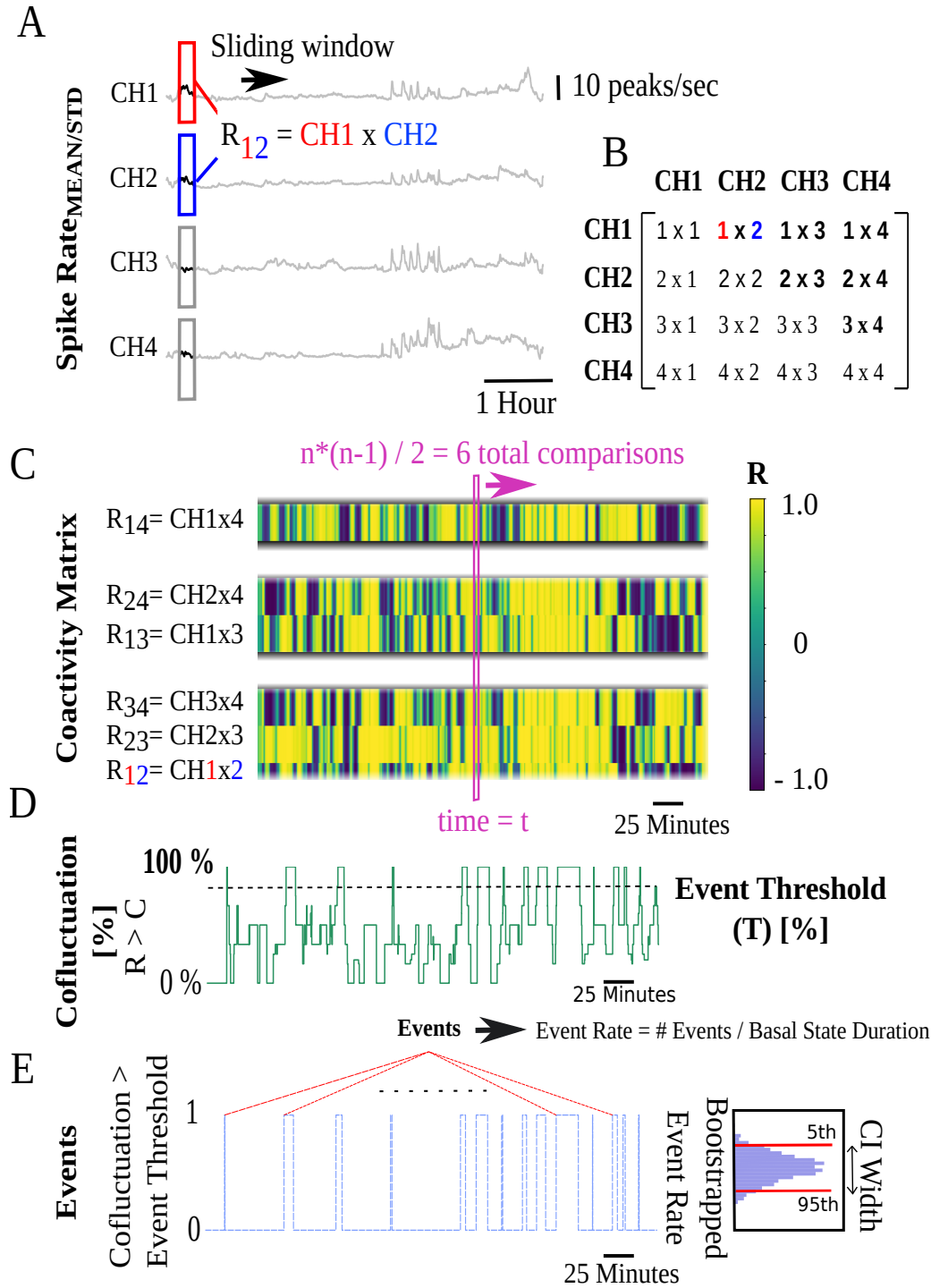


**Figure 8.** Coactivity matrix and event rate (ER) computation pipeline illustrated for 4-channels. A) Pearson's cross correlation coefficients ( $R$ ) of pairwise sliding spike rate windows for 4 channels. B)  $R$  values for cross correlation of 'i' and 'j' channels are stored in the 'i' and 'j' positions of a 4x4 matrix at each timestamp. C) Coactivity matrix super-diagonals at each timestamp are vertically stacked. At each timestamp  $t$ ,  $n(n-1)/2 = 6$  unique cross-correlations are possible corresponding to super-diagonals with 3, 2, and 1 members. The y-axis begins at the bottom with the 3 members of the first super-diagonal followed by subsequent super-diagonals. Colors represent the  $R$  value. D) Cofluctuation time series are the percentage of Pearson's  $R$  values at each timestamp that exceed a cofluctuation threshold ( $C$ ). E) Discrete events correspond to time intervals when cofluctuations show an up/down crossing through an event threshold ( $T$ ).

## Statistical Analysis

For variables that result in a single number per animal (such as  $ER_{MEAN}$  and  $ER_{STD}$ , Fig. 1A-B), independent samples t-tests or Wilcoxon rank-sum tests are respectively used for normal or non-normal data (normality assessed by Shapiro-Wilk) to quantify differences between animal groups.

For variables that have multiple variates per animal (such as  $Entropy_{MEAN}$  calculated from multiple channels, Fig. 1C-D), mixed effects models are constructed in the MATLAB Statistics and Machine Learning Toolbox (Pinheiro and Bates, 1996; MATLAB, 2021).  $Entropy_{MEAN}$  and similarly  $Entropy_{STD}$  (not shown) and  $Entropy_{MEAN,EVENT}$  and similarly  $Entropy_{STD,EVENT}$  (not shown) are modelled via mixed effects as, 1| indicates random effects,

$$Entropy_{MEAN} = Animal\ Type + (1|channel) + (1|animal\ ID) \quad (1)$$

$$Entropy_{MEAN,EVENT} = Event\ Type + Animal\ Type + CoactivityType + (1|channel) + (1|animal\ ID) + (1|Entropy_{MEAN}) \quad (2)$$

In Eq. (2), and depicted in Fig. 1C-D, the computed metric  $Entropy_{MEAN}$  is the outcome variable; the animal type (*control/HF*) a fixed effect; and the channel number (1 – 16) and the *animal ID* random effects. The analysis of  $Entropy_{STD}$  follows by replacing 'MEAN' with 'STD'.

In Eq. (2) the model  $Entropy_{MEAN,EVENT}$  is shown and refers to entropy mean data within event regions where the model for mean entropy data outside event regions is  $Entropy_{MEAN,NON-EVENT}$ . In this way, models are constructed for event / non-event, mean / std entropy as the outcome variable; the event type (event / non-event), the animal type (control / HF), and coactivity computation type (mean / std) are fixed effects; and channel number, animal ID, and entropy (type matching the outcome entropy's type, mean or std) are random effects.

For all analyses using mixed effects modeling, the  $\beta$  coefficients (fixed effects estimates),  $p$ -values, effect sizes ( $d_{RM}$  based on repeated measures Cohen's  $d_{RM}$ , (Lakens, 2013)), 95% confidence intervals ( $CI$ ) of  $\beta$  coefficients (lower, upper bounds) are reported in results in ( $\beta$ ,  $\pm CI$ ,  $d_{RM}$ ,  $p$ ) format. The  $\beta$  coefficients indicate the adjusted differences (units matching the outcome variable's unit) in one group compared to the other. For analyses with independent samples,  $p$ -values and independent samples effect sizes ( $d$ , based on Cohen's  $d$ ) are reported in ( $p$ ,  $d$ ) format. For all analyses, a two-sided  $p < 0.05$  denoted statistical significance.

## Acknowledgments

This work was funded by the National Institutes of Health, Office of The Director DP2 OD024323-01 and NHLBI R01 HL159001. NZG was funded by the National Science Foundation American Society of Engineering Education's Engineering Fellows Postdoctoral Fellowship Award ID #2127509. The authors would like to thank Prof. Jeffrey Ardell for fruitful discussions.

## References

- Ajijola OA, Chatterjee NA, Gonzales MJ, Gornbein J, Liu K, Li D, Paterson DJ, Shivkumar K, Singh JP, Herring N. Coronary sinus neuropeptide Y levels and adverse outcomes in patients with stable chronic heart failure. JAMA cardiology. 2020; 5(3):318–325.
- Ajijola OA, Lellouche N, Bourke T, Tung R, Ahn S, Mahajan A, Shivkumar K. Bilateral cardiac sympathetic denervation for the management of electrical storm. Journal of the American College of Cardiology. 2012; 59(1):91–92.
- Ajijola OA, Wisco JJ, Lambert HW, Mahajan A, Stark E, Fishbein MC, Shivkumar K. Extracardiac neural remodeling in humans with cardiomyopathy. Circulation: Arrhythmia and Electrophysiology. 2012; 5(5):1010–1116.
- Ajijola OA, Yagishita D, Patel KJ, Vaseghi M, Zhou W, Yamakawa K, So E, Lux RL, Mahajan A, Shivkumar K. Focal myocardial infarction induces global remodeling of cardiac sympathetic innervation: neural remodeling in a spatial context. American Journal of Physiology-Heart and Circulatory Physiology. 2013; 305(7):H1031–H1040.

367 **Ajijola OA**, Yagishita D, Reddy NK, Yamakawa K, Vaseghi M, Downs AM, Hoover DB, Ardell JL, Shivkumar K.  
368 Remodeling of stellate ganglion neurons after spatially targeted myocardial infarction: neuropeptide and  
369 morphologic changes. *Heart Rhythm*. 2015; 12(5):1027–1035.

370 **Akeju O**, Brown EN. Neural oscillations demonstrate that general anesthesia and sedative states are neuro-  
371 physiologically distinct from sleep. *Current opinion in neurobiology*. 2017; 44:178–185.

372 **Ardell J**, Andresen M, Armour J, Billman G, Chen PS, Foreman R, Herring N, O'leary D, Sabbah HN, Schultz HD,  
373 et al. Translational neurocardiology: preclinical models and cardioneural integrative aspects. *The Journal of*  
374 *physiology*. 2016; 594(14):3877–3909.

375 **Armour J**. Synaptic transmission in the chronically decentralized middle cervical and stellate ganglia of the dog.  
376 *Canadian journal of physiology and pharmacology*. 1983; 61(10):1149–1155.

377 **Armour J**. Activity of in situ stellate ganglion neurons of dogs recorded extracellularly. *Canadian journal of*  
378 *physiology and pharmacology*. 1986; 64(2):101–111.

379 **Armour J**, Collier K, Kember G, Ardell J. Differential selectivity of cardiac neurons in separate intrathoracic au-  
380 tonomic ganglia. *American Journal of Physiology-Regulatory, Integrative and Comparative Physiology*. 1998;  
381 274(4):R939–R949.

382 **Blaye-Felice MS**, Hamon D, Sacher F, Pascale P, Rollin A, Duparc A, Mondoly P, Derval N, Denis A, Cardin C,  
383 et al. Premature ventricular contraction-induced cardiomyopathy: related clinical and electrophysiologic  
384 parameters. *Heart Rhythm*. 2016; 13(1):103–110.

385 **Chamadia S**, Pedemonte JC, Hahm EY, Mekonnen J, Ibala R, Gitlin J, Ethridge BR, Qu J, Vazquez R, Rhee J, et al.  
386 Delta oscillations phase limit neural activity during sevoflurane anesthesia. *Communications biology*. 2019;  
387 2(1):1–10.

388 **Chen WW**, Xiong XQ, Chen Q, Li YH, Kang YM, Zhu GQ. Cardiac sympathetic afferent reflex and its implications  
389 for sympathetic activation in chronic heart failure and hypertension. *Acta Physiologica*. 2015; 213(4):778–  
390 794.

391 **Deyell MW**, Krahn AD, Goldberger JJ. Sudden cardiac death risk stratification. *Circulation research*. 2015;  
392 116(12):1907–1918.

393 **Esfahlani FZ**, Jo Y, Faskowitz J, Byrge L, Kennedy DP, Sporns O, Betzel RF. High-amplitude cofluctuations  
394 in cortical activity drive functional connectivity. *Proceedings of the National Academy of Sciences*. 2020;  
395 117(45):28393–28401.

396 **Gao L**, Pan YX, Wang WZ, Li YL, Schultz HD, Zucker IH, Wang W. Cardiac sympathetic afferent stimulation aug-  
397 ments the arterial chemoreceptor reflex in anesthetized rats. *Journal of Applied Physiology*. 2007; 102(1):37–  
398 43.

399 **Gao L**, Schultz HD, Patel KP, Zucker IH, Wang W. Augmented input from cardiac sympathetic afferents inhibits  
400 baroreflex in rats with heart failure. *Hypertension*. 2005; 45(6):1173–1181.

401 **Gurel NZ**, Sudarshan KB, Tam S, Ly D, Armour JA, Kember G, Ajijola OA. Studying Cardiac Neural Network  
402 Dynamics: Challenges and Opportunities for Scientific Computing. *Frontiers in Physiology*. 2022; p. 798.

403 **Gutierrez-Barragan D**, Singh NA, Alvino FG, Coletta L, Rocchi F, De Guzman E, Galbusera A, Uboldi M, Panzeri S,  
404 Gozzi A. Unique spatiotemporal fMRI dynamics in the awake mouse brain. *Current Biology*. 2022; 32(3):631–  
405 644.

406 **Han S**, Kobayashi K, Joung B, Piccirillo G, Maruyama M, Vinters HV, March K, Lin SF, Shen C, Fishbein MC, et al.  
407 Electroanatomic remodeling of the left stellate ganglion after myocardial infarction. *Journal of the American*  
408 *College of Cardiology*. 2012; 59(10):954–961.

409 **Hori Y**, Temma T, Wooten C, Sobowale C, Chan C, Swid M, Ajijola OA. Cardiac afferent signaling partially under-  
410 lies premature ventricular contraction-induced cardiomyopathy. *Heart Rhythm*. 2021; 18(9):1586–1595.

411 **Hultman R**, Ulrich K, Sachs BD, Blount C, Carlson DE, Ndubuizu N, Bagot RC, Parise EM, Vu MAT, Gallagher NM,  
412 et al. Brain-wide electrical spatiotemporal dynamics encode depression vulnerability. *Cell*. 2018; 173(1):166–  
413 180.

414 **Kember G**, Armour JA, Zamir M. Neural control hierarchy of the heart has not evolved to deal with myocardial  
415 ischemia. *Physiological genomics*. 2013; 45(15):638–644.

**Lakens D.** Calculating and reporting effect sizes to facilitate cumulative science: a practical primer for t-tests and ANOVAs. *Frontiers in psychology*. 2013; p. 863.

**Ma R, Zucker IH, Wang W.** Central gain of the cardiac sympathetic afferent reflex in dogs with heart failure. *American Journal of Physiology-Heart and Circulatory Physiology*. 1997; 273(6):H2664–H2671.

**Mague SD, Talbot A, Blount C, Walder-Christensen KK, Duffney LJ, Adamson E, Bey AL, Ndubuizu N, Thomas GE, Hughes DN, et al.** Brain-wide electrical dynamics encode individual appetitive social behavior. *Neuron*. 2022; 110(10):1728–1741.

**MATLAB.** version 7.10.0 (R2010a). Natick, Massachusetts: The MathWorks Inc.; 2021.

**Mehra R, Tjurmina OA, Ajijola OA, Arora R, Bolser DC, Chapleau MW, Chen PS, Clancy CE, Delisle BP, Gold MR, et al.** Research Opportunities in Autonomic Neural Mechanisms of Cardiopulmonary Regulation: A Report From the National Heart, Lung, and Blood Institute and the National Institutes of Health Office of the Director Workshop. *JACC: Basic to Translational Science*. 2022; .

**Miller JeK, Ayzenshtat I, Carrillo-Reid L, Yuste R.** Visual stimuli recruit intrinsically generated cortical ensembles. *Proceedings of the National Academy of Sciences*. 2014; 111(38):E4053–E4061.

**Nakamura K, Ajijola OA, Aliotta E, Armour JA, Ardell JL, Shivkumar K.** Pathological effects of chronic myocardial infarction on peripheral neurons mediating cardiac neurotransmission. *Autonomic Neuroscience*. 2016; 197:34–40.

**Pinheiro JC, Bates DM.** Unconstrained parametrizations for variance-covariance matrices. *Statistics and computing*. 1996; 6(3):289–296.

**Sudarshan KB, Hori Y, Swid MA, Karavos AC, Wooten C, Armour JA, Kember G, Ajijola OA.** A novel metric linking stellate ganglion neuronal population dynamics to cardiopulmonary physiology. *American Journal of Physiology-Heart and Circulatory Physiology*. 2021; 321(2):H369–H381.

**Vaseghi M, Barwad P, Malavassi Corrales FJ, Tandri H, Mathuria N, Shah R, Sorg JM, Gima J, Mandal K, Sàenz Morales LC, et al.** Cardiac sympathetic denervation for refractory ventricular arrhythmias. *Journal of the American College of Cardiology*. 2017; 69(25):3070–3080.

**Vaseghi M, Zhou W, Shi J, Ajijola OA, Hadaya J, Shivkumar K, Mahajan A.** Sympathetic innervation of the anterior left ventricular wall by the right and left stellate ganglia. *Heart rhythm*. 2012; 9(8):1303–1309.

**Virtanen P, Gommers R, Oliphant TE, Haberland M, Reddy T, Cournapeau D, Burovski E, Peterson P, Weckesser W, Bright J, et al.** SciPy 1.0: fundamental algorithms for scientific computing in Python. *Nature methods*. 2020; 17(3):261–272.

**Wagner MJ, Savall J, Hernandez O, Mel G, Inan H, Romyantsev O, Lecoq J, Kim TH, Li JZ, Ramakrishnan C, et al.** A neural circuit state change underlying skilled movements. *Cell*. 2021; 184(14):3731–3747.

**Wang HJ, Rozanski GJ, Zucker IH.** Cardiac sympathetic afferent reflex control of cardiac function in normal and chronic heart failure states. *The Journal of physiology*. 2017; 595(8):2519–2534.

**Wang HJ, Wang W, Cornish KG, Rozanski GJ, Zucker IH.** Cardiac sympathetic afferent denervation attenuates cardiac remodeling and improves cardiovascular dysfunction in rats with heart failure. *Hypertension*. 2014; 64(4):745–755.

**Wang W, Zucker IH.** Cardiac sympathetic afferent reflex in dogs with congestive heart failure. *American Journal of Physiology-Regulatory, Integrative and Comparative Physiology*. 1996; 271(3):R751–R756.

**Wang WZ, Gao L, Wang HJ, Zucker IH, Wang W.** Interaction between cardiac sympathetic afferent reflex and chemoreflex is mediated by the NTS AT1 receptors in heart failure. *American Journal of Physiology-Heart and Circulatory Physiology*. 2008; 295(3):H1216–H1226.

**Yoshie K, Rajendran PS, Massoud L, Kwon O, Tadimeti V, Salavatian S, Ardell JL, Shivkumar K, Ajijola OA.** Cardiac vanilloid receptor-1 afferent depletion enhances stellate ganglion neuronal activity and efferent sympathetic response to cardiac stress. *American Journal of Physiology-Heart and Circulatory Physiology*. 2018; 314(5):H954–H966.

**Yoshie K, Rajendran PS, Massoud L, Mistry J, Swid MA, Wu X, Sallam T, Zhang R, Goldhaber JL, Salavatian S, et al.** Cardiac TRPV1 afferent signaling promotes arrhythmogenic ventricular remodeling after myocardial infarction. *JCI insight*. 2020; 5(3).

**Animation 1: Entropy Animation.** The Animation 1.gif file contains an animation of the building of the neural specificity metric with respect to left ventricular pressure (LVP).

**Row 1:** Computation of the neural specificity metric for different frames is shown in the form of 20 second moving windows on a 45s segment of the LVP data. The LVP data is shown in blue tracings with the neural spikes represented as red dots.

**Row 2:** Two normalized histograms for each of the moving windows are calculated and shown in the second row. The histogram of the LVP computed at spike times (Neurally sample LVP) is on the left. The histogram of the LVP in the window (randomly sampled LVP) is on the right.

**Row 3:** The computed histograms are then used to compute two matrices in the third row. The matrices contain all the corresponding histograms computed in the previous step arranged vertically with a hard threshold of 0.5 applied i.e., histogram values greater than 0.5 are set to 0.5 (Colored yellow).

**Row 4:** The two matrices computed in row 3 are subtracted to obtain the neural specificity metric shown in the fourth row. The color scheme is explained in Fig. 4 in Appendix 1 of the manuscript.

**Row 5:** Entropy shown in the fifth row is obtained by calculating the Shannon entropy (such as depicted in Fig. 4) for the subtracted histogram in each of the moving windows for the duration of the metric.

## Appendix 1

### Cofluctuation and Event Rate Definitions

#### Coactivity Matrix

A 16x16 correlation matrix, 4x4 version is shown in Fig. 8B for  $n = 4$  channels, is used to investigate spatial coherence among neural populations in different regions of the SG spanned by 16 electrodes (Fig. 1). The coactivity matrix at each timestamp is found from Pearson's cross-correlation between all possible pairs of spike rate, causal channel, sliding mean and standard deviation. The sliding mean and standard deviation of spike rate are  $Spike_{RateMEAN}$  and  $Spike_{RateSTD}$ , and are on the y-axis of Fig. 8A. These are referred to as 'spike rate' in what follows when both are implied. To fix ideas, consider Pearson's cross correlation coefficient ( $R$ ) between channels 1 and 2, labeled as  $R_{12}$ : namely, the red and blue windows respectively in Fig. 8A. In the coactivity matrix depicted in Fig. 8B, there are  $n = 4$  channels, hence  $n - 1 = 3$  super-diagonals. These are vertically stacked in Fig. 8C at each timestamp beginning with the first super-diagonal as  $R_{12}$ ,  $R_{23}$ ,  $R_{34}$ . In this way, adjacent channels are placed at the bottom followed by super-diagonals corresponding to 2 and 3 channels of separation. The super-diagonal of the 16-channel LMA electrode correlation matrix has  $n = 16$  channels separated by  $500\mu m$  and  $n(n - 1)/2 = 120$  possible pairwise correlations (See Fig. 5 for an example). This yields 120 rows in the stacked version of the coactivity matrix at each timestamp analogous to the same visualized in Fig. 8C for  $n = 4$  channels.

#### Cofluctuations and Event Rate

The univariate cofluctuation time series is the percentage of coactivity matrix members, at each timestamp, that exceed a threshold Pearson's  $R > C$ , depicted in Fig. 8D. Discrete events are considered to begin at a time of up-crossing of the univariate cofluctuation time series through a threshold  $T$ . Each event ends at a down-crossing some time later, as shown in Fig. 8E. These discrete events capture spatiotemporal zones of high SG coactivity. Up-crossing times are respectively converted to an event rate ( $ER_{MEAN}, ER_{STD}$ ) for the ( $Spike_{RateMEAN}, Spike_{RateSTD}$ ) over a duration

$$(ER_{MEAN}, ER_{STD}) = \frac{(N_{MEAN}, N_{STD})}{EventsDuration} \quad (A.1)$$

where event rate,  $ER$ , has units  $1/s$  and ( $N_{MEAN}, N_{STD}$ ) are the number of upcrossings within the  $EventsDuration$  considered.

#### Cofluctuation Probability Distribution

The cofluctuation time series at each threshold  $C$  (as in Fig. 8D) qualitatively approximates a log-normal distribution. The log-normal fits of cofluctuation time series (Fig. 2) are obtained using Python SciPy package, with statistics and random numbers module (scipy.stats) (Virtanen et al., 2020).



## Bootstrapping and Selection of Convergent Thresholds

The event rate is calculated based on a pair of thresholds  $(C, T)$ . The first threshold  $C$  (Fig. 8D) is used to reduce the coactivity time series of matrices to a univariate coactivity time series. The univariate series is the percentage of coactivity matrix entries exceeding  $C$  at each timestamp. The coactivity time series is then used to define regions of high coactivity based on intervals where the time series exceeds a second threshold  $T$ . These regions are discrete 'events' that begin and end when the coactivity time series respectively up- and down-crosses through  $T$  (Fig. 8D). Bootstrapping of the event up-crossing timestamps is used to construct the event rate histogram of a threshold pair  $(C, T)$ .

These histograms lead to a convergent choice of threshold pairs  $(C, T)$ . The convergent  $(C, T)$  pair is taken as the location in  $(C, T)$  space where the confidence interval (CI) width shows apparent convergence. An upper bound on  $(C, T)$  is imposed so that there is sufficient data to compute the desired statistics.

The procedure is visualized in Fig. 1A using a surrogate coactivity matrix  $R$ . Univariate coactivity time series are created from a range of thresholds  $C$  that inclusively vary over 60-90% with 15% increments. Discrete events are determined, shown as red up-crossing triangles in Fig. 1 A-B, for each of the thresholds  $C$  and considered over an inclusive range 40-90% with 10% increments of event thresholds  $T$ . Bootstrapped events provided the associated  $ER$  histogram of each  $(C, T)$  threshold pair and desired 95% CI width of each animal (Fig. 2A). A convergent  $(C, T)$  pair for an animal is provided in Fig. 2B ( $C, T = 0.9, 90$ ), that converged to a 95% CI width of 0.005. Following this approach, convergent  $(C, T)$  pairs and bootstrapped CI widths are listed for each animal in Fig. 2C.

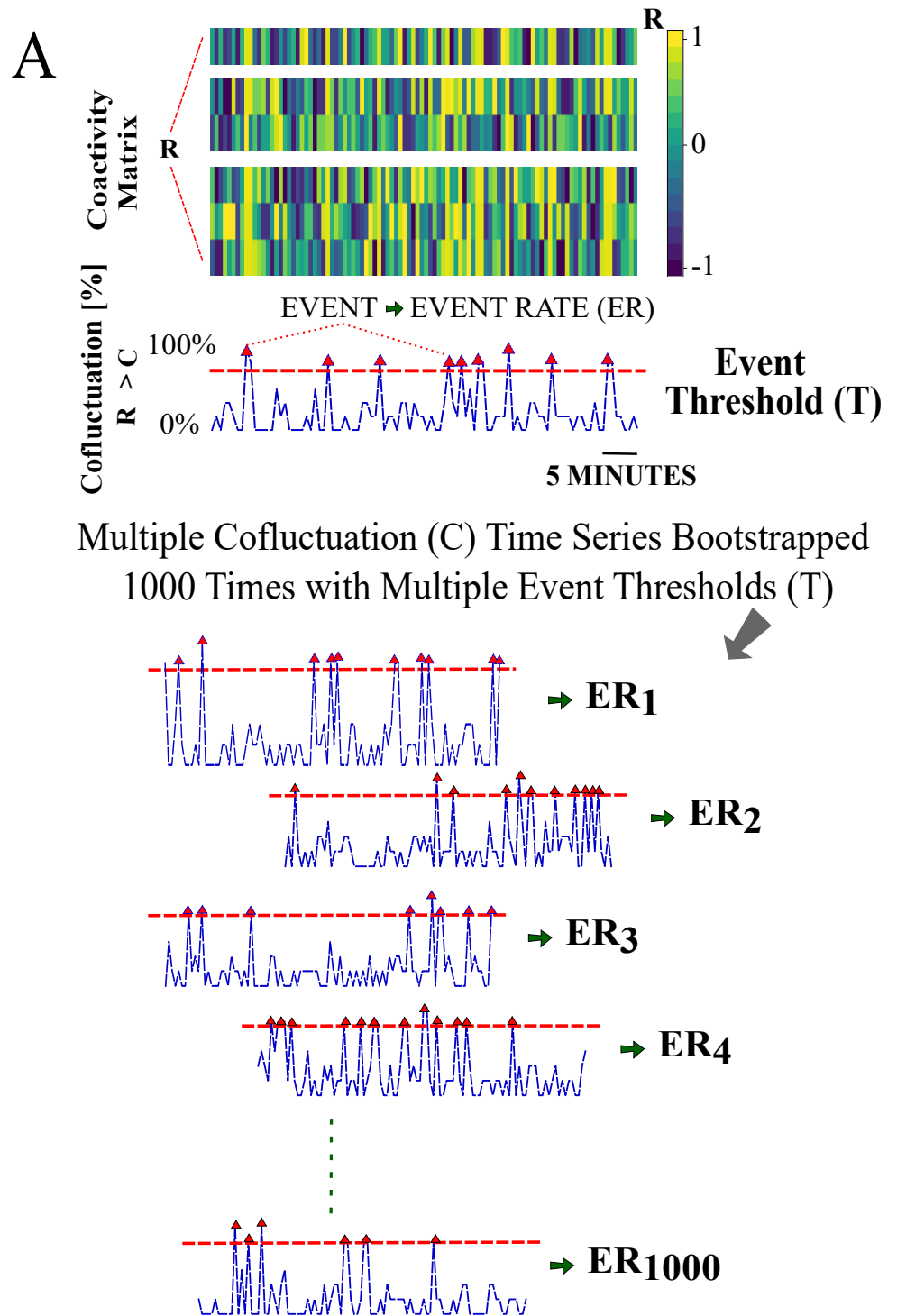
Using these individualized convergent  $(C, T)$  pairs, original (i.e., not bootstrapped) data are used to calculate event rates for each animal. Note that event rates are calculated from both spike rate mean and standard deviation coactivity matrices, and referred to as  $ER_{MEAN}$  and  $ER_{STD}$ . These are then used in statistical analyses (one  $ER_{MEAN}$  and one  $ER_{STD}$  per animal) as shown in Fig. 7. A similar procedure was performed in the literature using neuroimaging time series data based on Pearson's  $R$  (Esfahlani et al., 2020) however the threshold selection process was qualitative. In this work, we have developed a quantitative approach for threshold selection.

## Neural Specificity

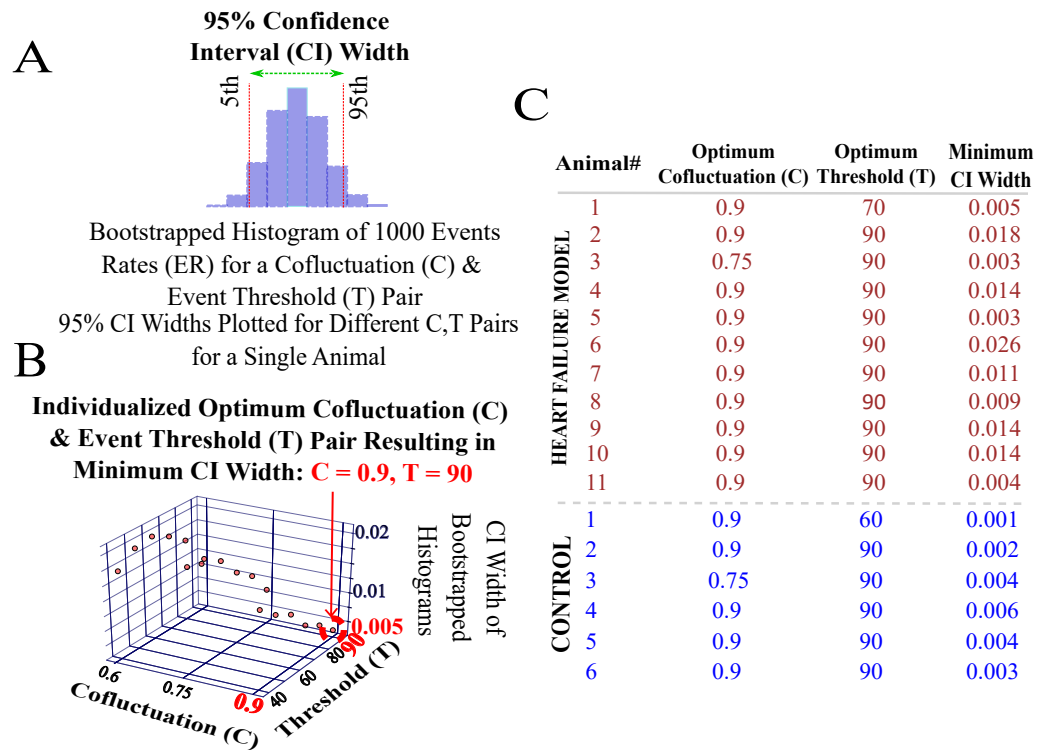
The neural specificity metric (Sudarshan et al., 2021), Figs. 3 and 4, is used to evaluate the degree to which neural activity is biased toward control target states taken here as LVP. Briefly, this metric is computed in three stages

1. *Neural Sampling* The value of the target state (LVP) is 'sampled' at the timestamp of each spike occurrence. This sampling is assumed to approximate a quasi-stationary distribution over a causal (backward in time) sliding window of spiking activity that is updated at each new timestamp. The distribution is approximated as a normalized and sliding histogram of neurally sampled target states (LVP).
2. *Random Sampling* The normalized, sliding random sampling histogram is found at each spike occurrence in (1), but based on *all* available LVP samples within the same causal window referenced in (1), which approximates the random sampling limit.
3. *Neural Specificity* The normalized, sliding random sampling histogram (2) is subtracted from its neural sampling counterpart (1) to form the neural specificity contrastive measure.

Subtraction of the random sampling histogram from the neural sampling histogram allows for the discovery of the degree to which neural activity is biased, or specific, toward sampling control target states (LVP here) relative to random sampling. To explain the construction of the metric with LVP, a representative window is shown in Fig. 3A with the spikes shown as green dots over LVP waveform. The following steps outline the construction of the neural specificity metric,  $A$ , for a representative LVP window



**Appendix 1 Figure 1.** Cofluctuation bootstrapping pipeline for individualized event rate (ER) for each animal - Part I. A) Coactivity matrix and cofluctuation time series for a cofluctuation threshold and event threshold pair ( $C, T$ ). B) Cofluctuation time series with depicted events (red triangles are upcrossing timestamps) for a range of ( $C, T$ ) pairs. Fig. 1A is further explained in Appendix 1 Figure labelled as Fig. A5.



**Appendix 1 Figure 2.** Cofluctuation bootstrapping pipeline for individualized event rate (ER) for each animal - Part II. A) Bootstrapped histogram of ERs for a single (C, T) pair with 95% confidence interval (CI) width. B) Threshold pair (C, T) is chosen for an animal given non-zero ER and ER convergence. Depicted CI widths are found at all of the depicted 18 (C, T) pairs available on the axes grid. C) List of (C, T) pairs that show ER convergence with CI widths for each animal.

546 1. *Neural Sampling*

547 Following (*Sudarshan et al., 2021*), the normalized sliding window histogram of neurally sam-  
 548 pled  $LVP_j$  at all spike times  $t_j$  and taken over  $M$  bins is defined for bin  $k$  as

$$H(SLVP_j)_k = \frac{h(SLVP_j)_k}{\sum_{k=1}^{k=m} h(SLVP_j)_k} \quad (\text{A.2})$$

549 Eq. (A.2) approximates the distribution of neural sampling of the target LVP at the green  
 550 dots over a causal window in Fig. 3A. The resulting normalized histogram shown for one  
 551 timestamp (green line) in Fig. 3B.

552 2. *Random Sampling* The normalized sliding window histogram at the random sampling limit of  
 553  $LVP_j$  is computed as in (1), but based on *all* LVP samples within the same causal window  
 554 and defined as  $H(LVP_j)_k$ . This is depicted as sampling of the pink line in Fig. 3A over the  
 555 same causal window used to describe neural sampling of LVP. The result is shown for one  
 556 timestamp as the normalized histogram (pink line) in Fig. 3B.

557 3. *Neural Specificity* The neural specificity,  $A_{jk}$ , for bin  $k$  is

$$A_{jk} = H(SLVP_j)_k - H(LVP_j)_k \quad (\text{A.3})$$

558  $A_{jk}$  is mapped to three levels (*less, same, greater*) relative to random sampling. These are  
 559 respectively defined as  $(-1, 0, 1)$  and depicted as (*purple, teal, yellow*) in Fig. 3C and 4A. As  
 560 such, given the mapping threshold  $\alpha > 0$  it follows that  $(A_{jk} < -\alpha, A_{jk} < \alpha, A_{jk} > \alpha)$  is respec-  
 561 tively  $(-1, 0, 1)$  implying (*less, same, greater*) neural specificity relative to random sampling and  
 562 visually represented as (*purple, teal, yellow*).

563 **Entropy Definitions**

564 **Entropy**

565 The neural specificity is reduced from a multivariate signal to a univariate signal by computing the  
 566 Shannon entropy at each timestamp of the mapped neural specificity metric (Fig. 7), Eq. (A.3) map-  
 567 ping description). The entropy of the absolute change between adjacent normalized histogram  
 568 bins is a measure of coherence in neural specificity. The absolute change in the mapped  $A_{jk}$  at  
 569 time  $t_j$  and between adjacent bins  $(k, k + 1)$ ,  $k = 1, \dots, m - 1$  is the set  $\Delta A_j = (0, 1, 2)$  with members  
 570  $\Delta A_{ji}, i = 1, 2, 3$ . Using a base 3 logarithm to scale the entropy between 0 and 1, the entropy  $E_j$  of  
 571 the difference in the mapped  $A_{jk}$  at each timestamp  $t_j$ .

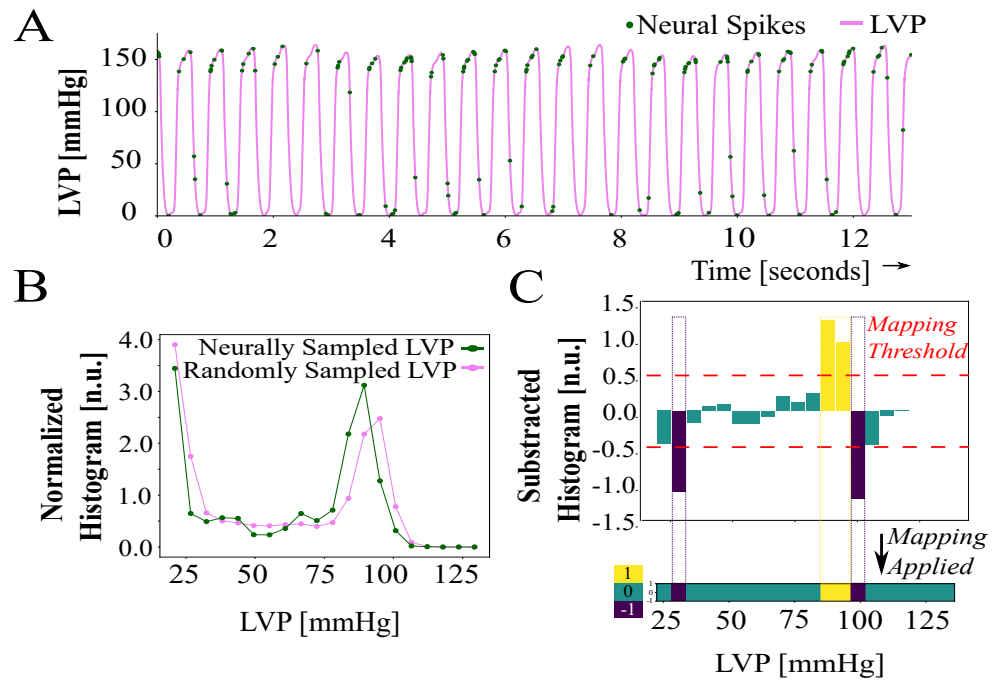
$$E_j = -\sum_{\Delta A_{ji}=1}^3 p(\Delta A_{ji}) \ln_3(p(\Delta A_{ji})) \quad (\text{A.4})$$

572 This unequally-sampled series is interpolated to the equally-sampled time series  $E$ .

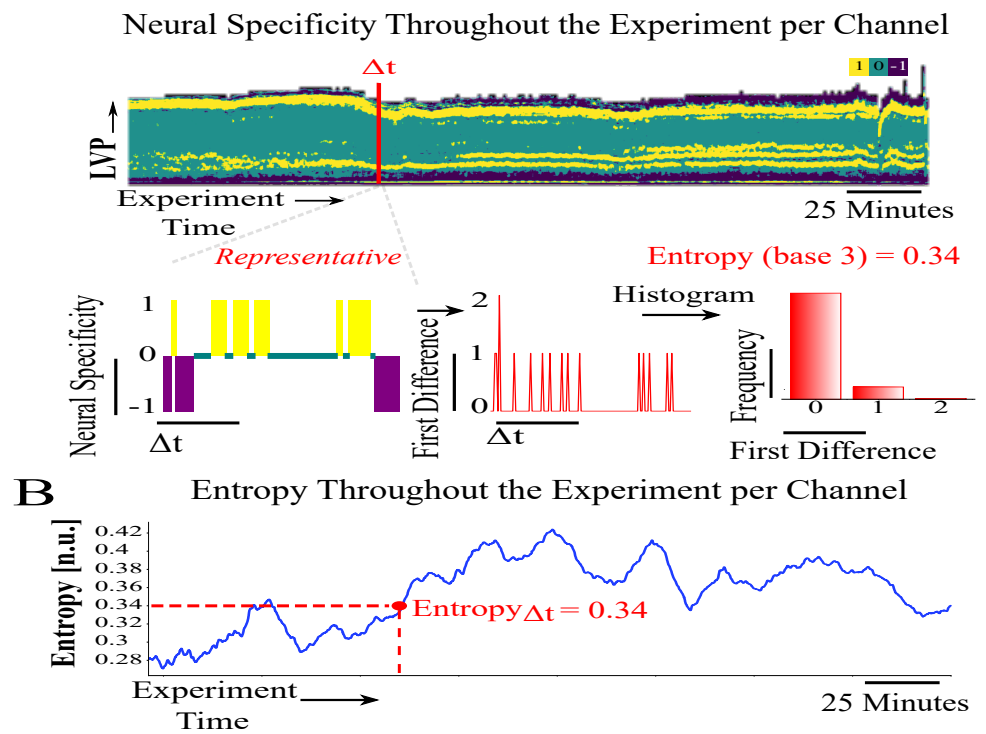
573 **Event Entropy**

574 The neural specificity is a measure of specificity, or bias, of neural activity to target states. However,  
 575 unusually high and short-lived cofluctuations indicate intervals in time, or ‘events’, when coactivity  
 576 between channel pairs implies that SG processing has undergone sudden changes. Functional  
 577 relevance of cofluctuation events is found by considering the extent to which neural specificity to  
 578 the target (LVP here) is similar or different inside and outside these events.

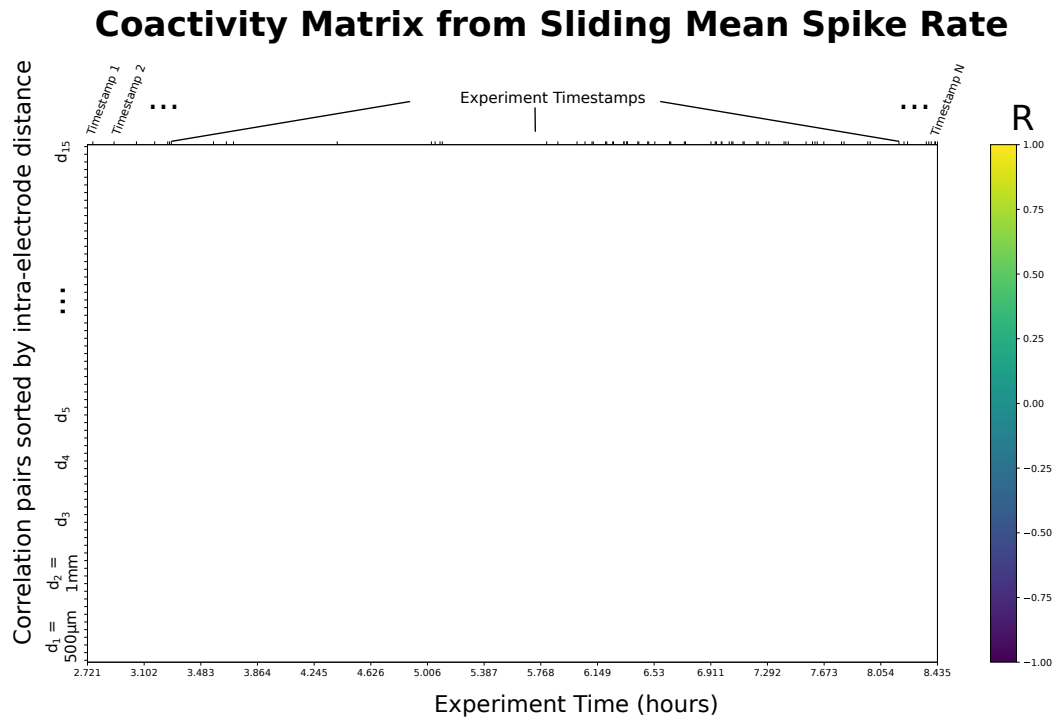
579 Therefore, the functional relevance of cofluctuations in SG neural activity is examined by break-  
 580 ing the time-evolution of entropy of neural specificity into regions: ‘event’ regions (within event  
 581 intervals) and ‘non-event’ regions (outside event intervals). The mean and standard deviation of  
 582 event and non-event entropy time series per channel are computed for each experiment and col-  
 583 lectively referred to as ‘event entropy’ where this is convenient.



**Appendix 1 Figure 3.** Neural specificity and entropy computation - Part I. A) Neural specificity sample showing left ventricular pressure (LVP) and neural spikes. Spiking activity is more specific or biased (yellow), over random sampling, to LVP just below systolic pressures. B) Normalized histograms of random and neurally sampled LVP. C) Bars show subtracted histograms and colors indicate the specificity thresholded with  $\alpha = 0.5$ : specificity exceeding  $\alpha$  is yellow, below  $-\alpha$  is blue, and between the bounds  $(-\alpha, \alpha)$  is teal.

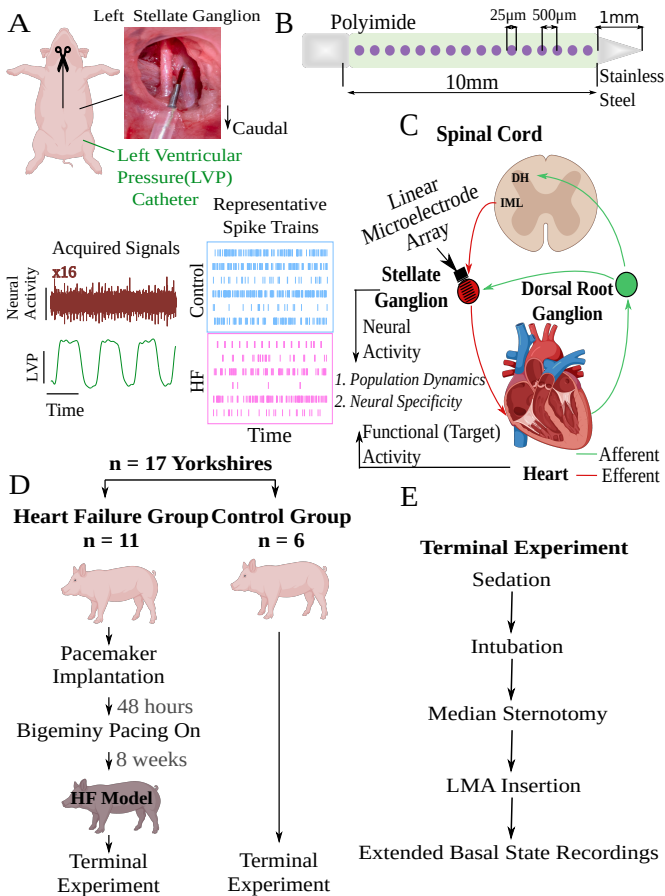


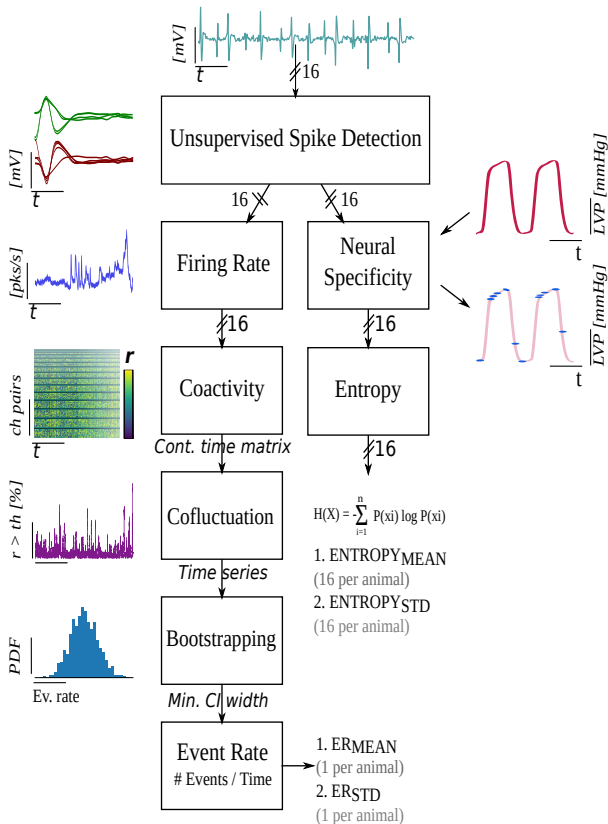
**Appendix 1 Figure 4.** Neural specificity and entropy computation - Part II. A) Sliding neural specificity time series (top) for a selected sliding window width  $\Delta t$ . Entropy of neural specificity, computed from red highlighted window of width  $\Delta t$ , absolute difference (shown for a sample at bottom). B) Entropy time series corresponding to the overall experiment, entropy sample computed from steps in D. An animated version is in Animation 1.



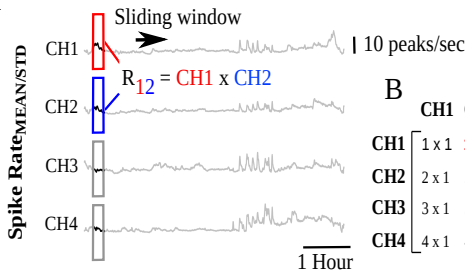
**Appendix 1 Figure 5. 16-Channel Version of Fig. 1A.** A sample coactivity matrix computed from the sliding (rolling) mean of spike rate for the 16-channel linear mapping array (LMA) used throughout an experiment. Y axis shows correlation pairs (i.e., Channel 1 vs. Channel 2). Correlation pairs are stacked such that the lowest row corresponds to channels separated by the minimum inter-electrode distance ( $d_1 = 500\mu m$ , 1-electrode away), and inter-electrode distance increasing from a separation of 1 to 15 channels at the top. For instance, the highest row shows the pair separated by the maximum inter-electrode distance ( $d_{15} = 15 * 500\mu m = 7.5mm$ , 15-electrodes away). The order corresponds to the super-diagonals of the 16 x 16 correlation matrix. Y axis includes 120 comparisons for 16 channels, colors indicate Pearson's correlation coefficients specified in the color legend.







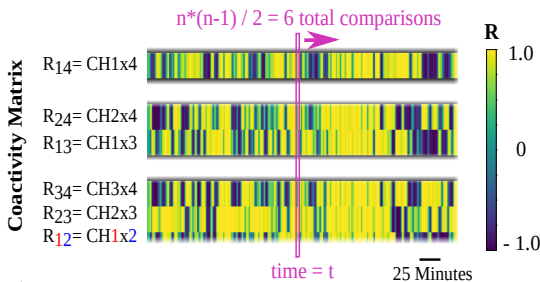
A



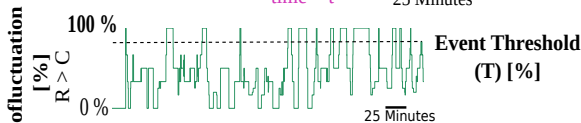
B

	CH1	CH2	CH3	CH4
CH1	1 x 1	1 x 2	1 x 3	1 x 4
CH2	2 x 1	2 x 2	2 x 3	2 x 4
CH3	3 x 1	3 x 2	3 x 3	3 x 4
CH4	4 x 1	4 x 2	4 x 3	4 x 4

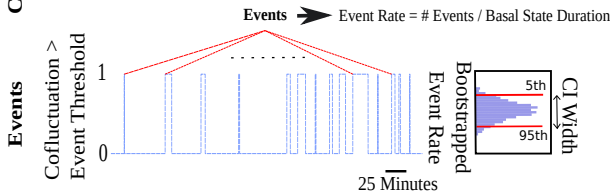
C



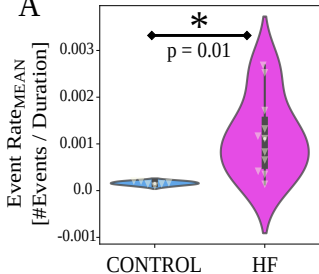
D



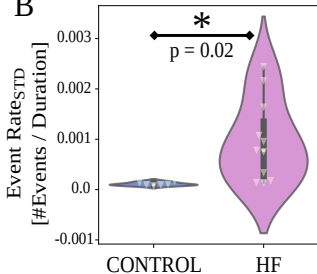
E



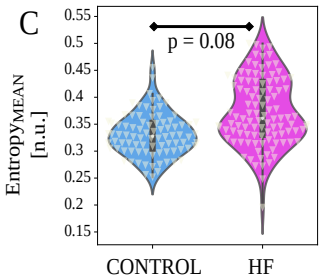
A



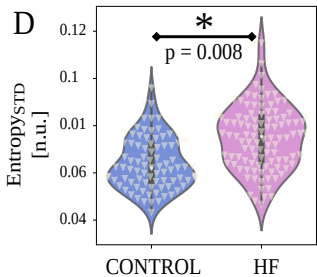
B



C



D

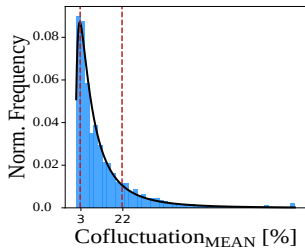


## Control Group

Log-normal Fit —  
68% CI bounds - - -

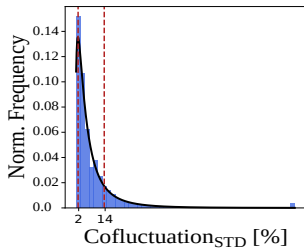
A

$\mu_{FIT} = 13, \sigma_{FIT} = 18$



B

$\mu_{FIT} = 8, \sigma_{FIT} = 11$

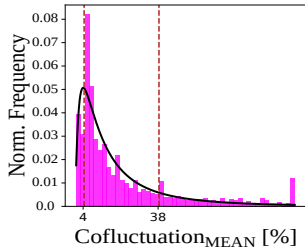


## HF Group

Log-normal Fit —  
68% CI bounds - - -

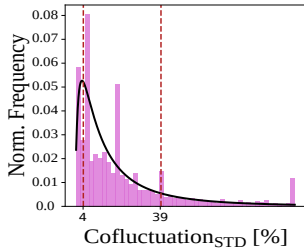
C

$\mu_{FIT} = 23, \sigma_{FIT} = 35$



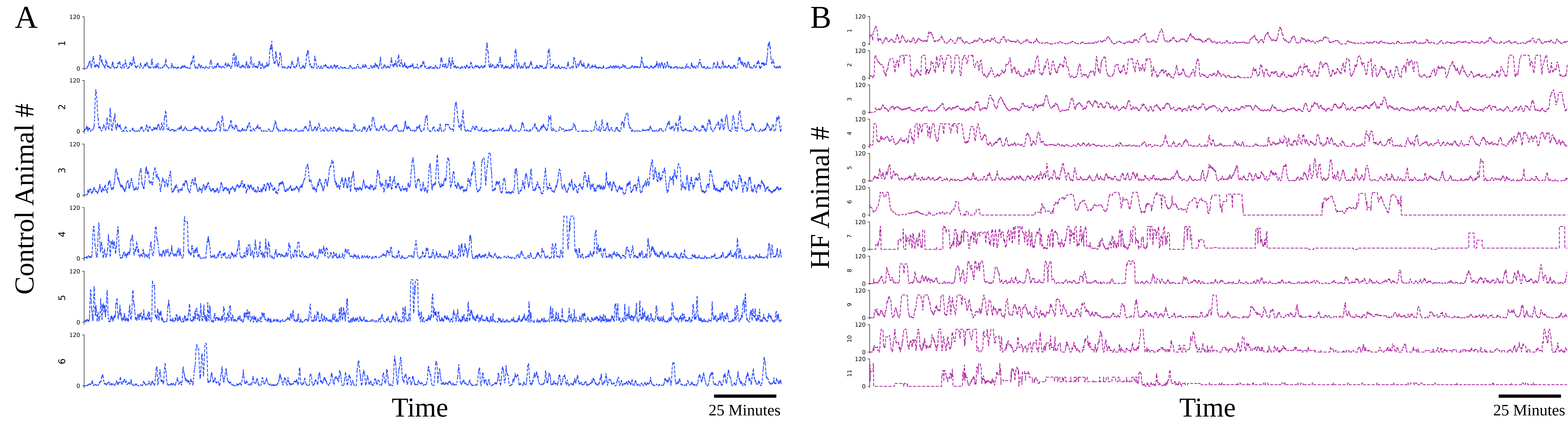
D

$\mu_{FIT} = 24, \sigma_{FIT} = 39$

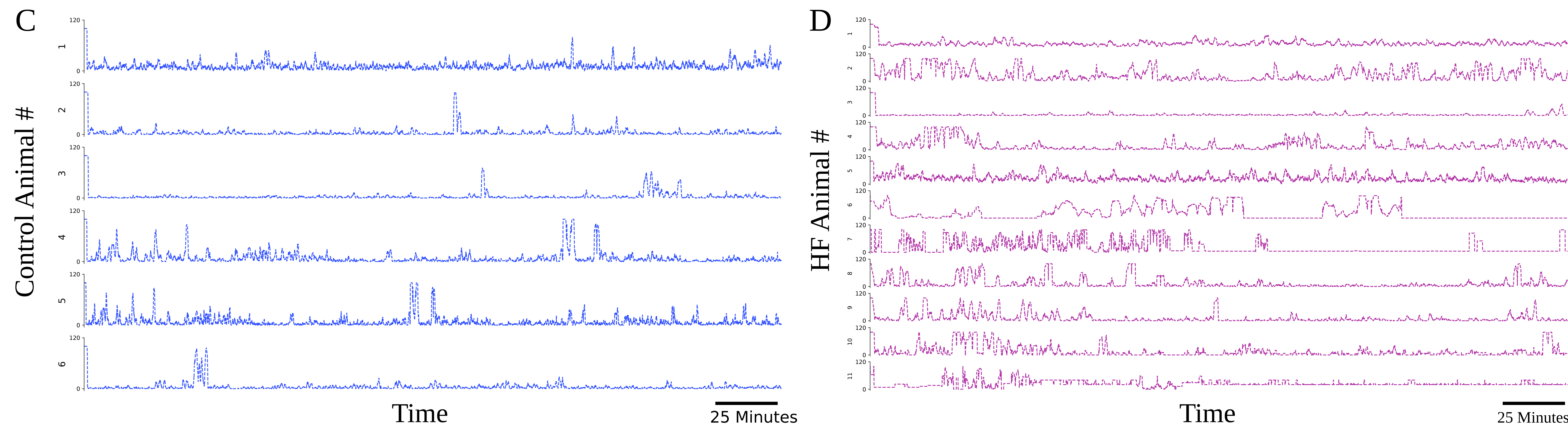




# Cofluctuations Computed from Spike Rate<sub>MEAN</sub>

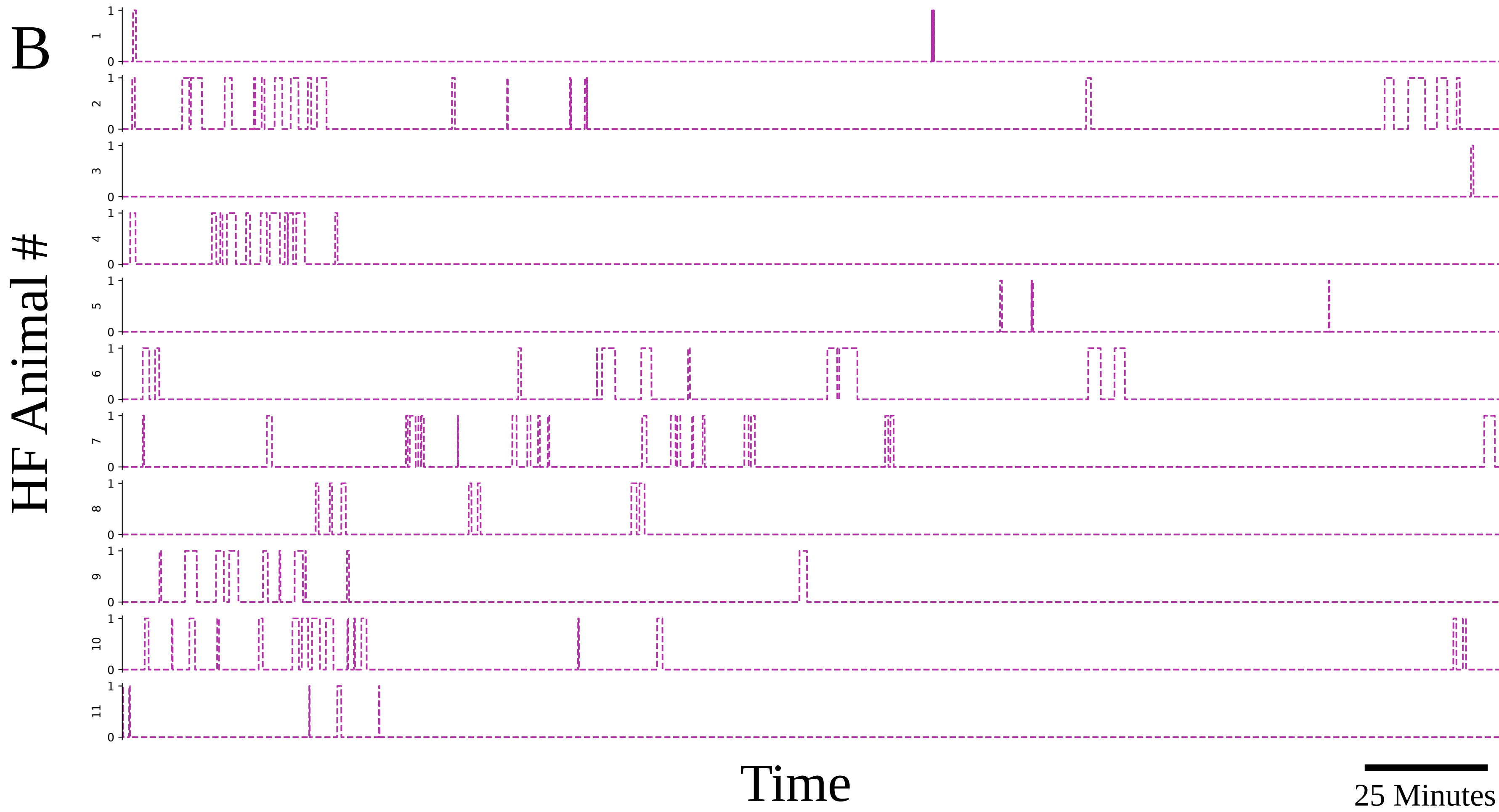
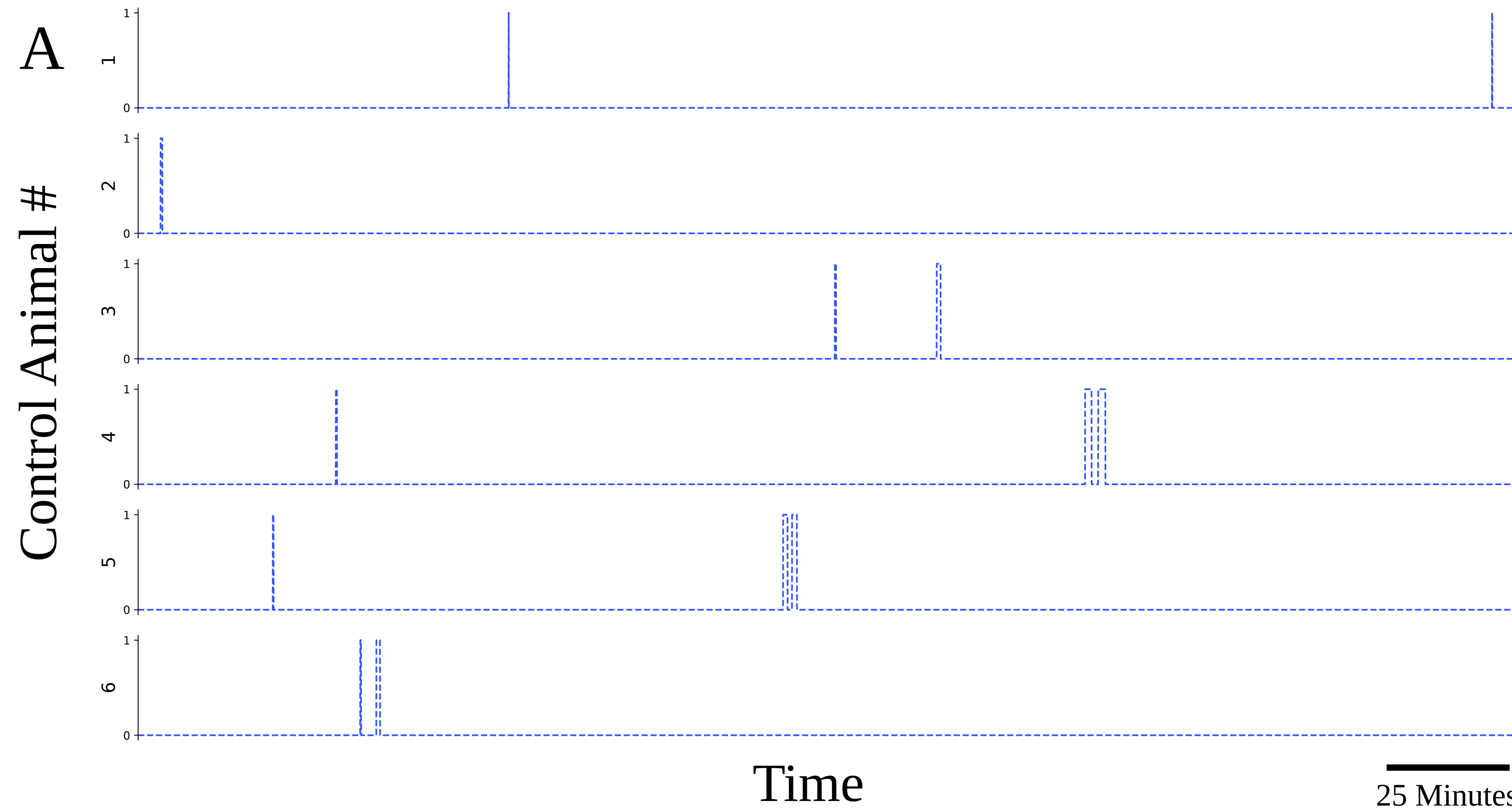


# Cofluctuations Computed from Spike Rate<sub>STD</sub>

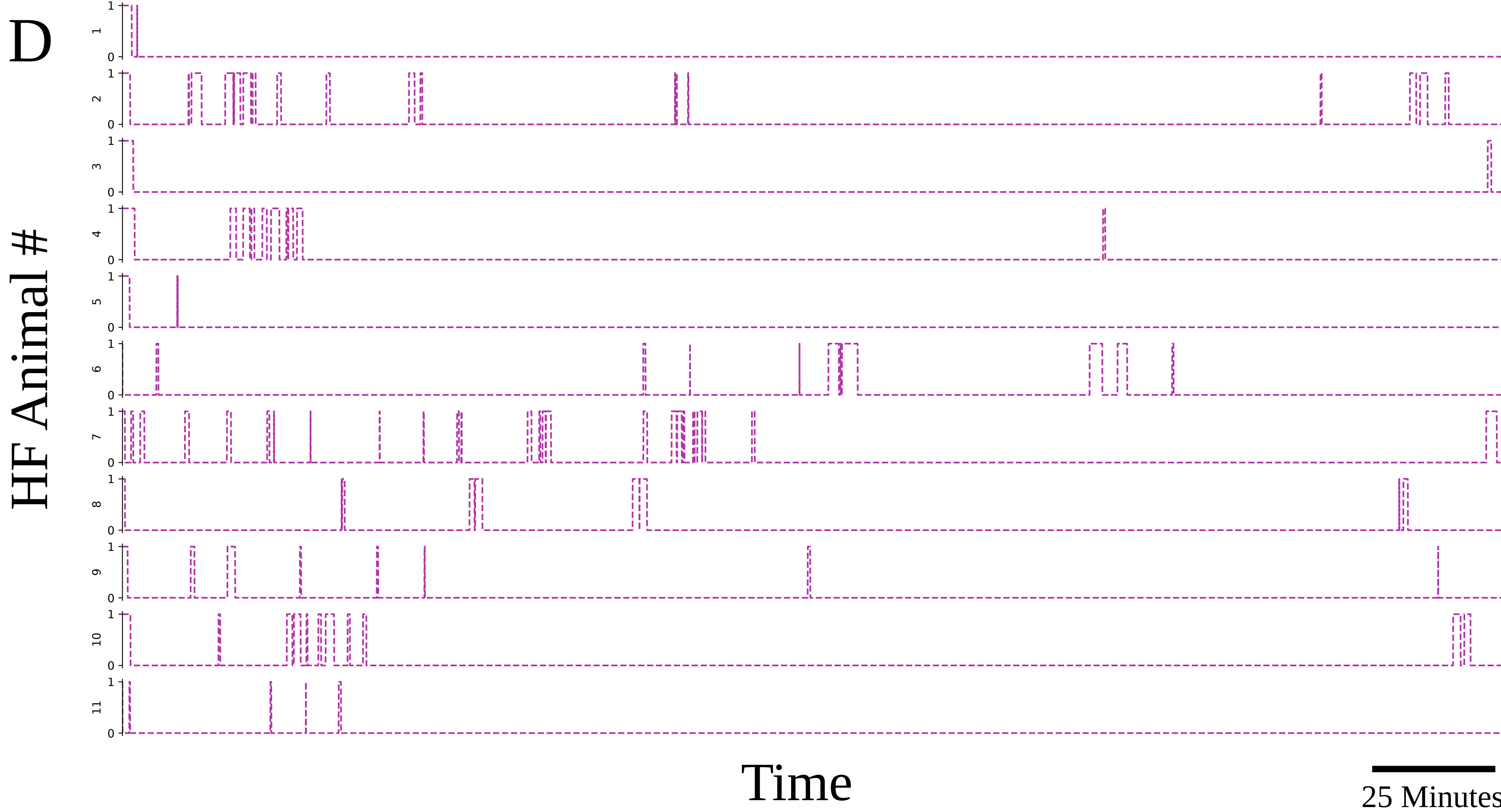
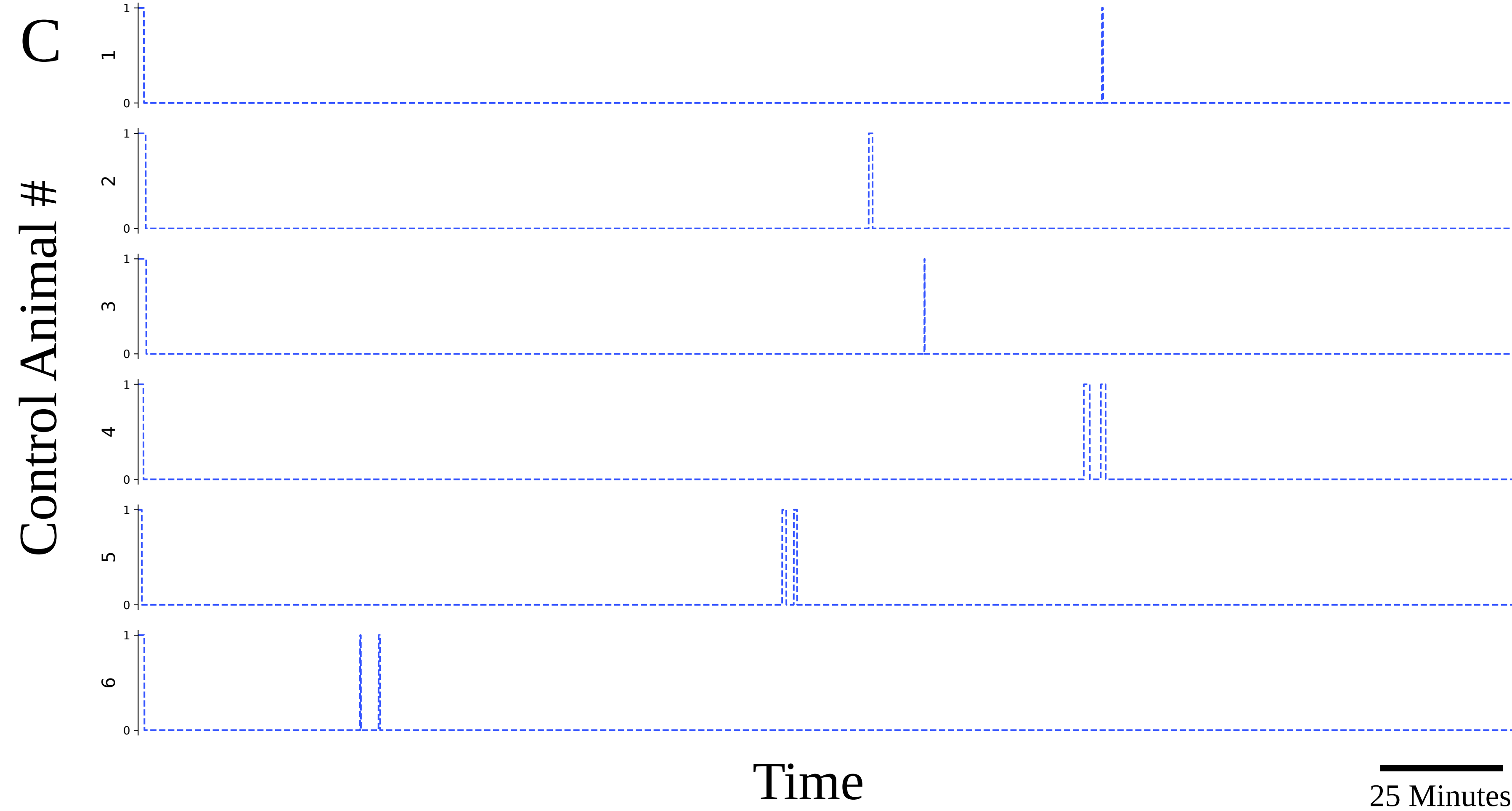




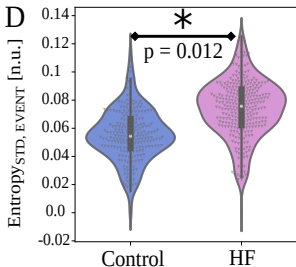
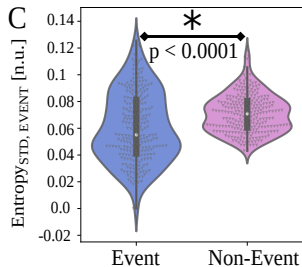
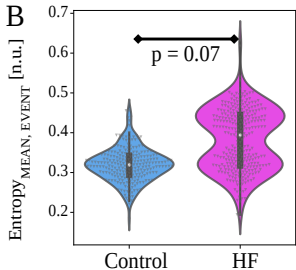
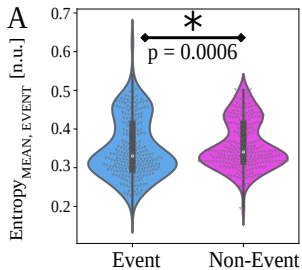
Events Computed from Spike Rate<sub>MEAN</sub>

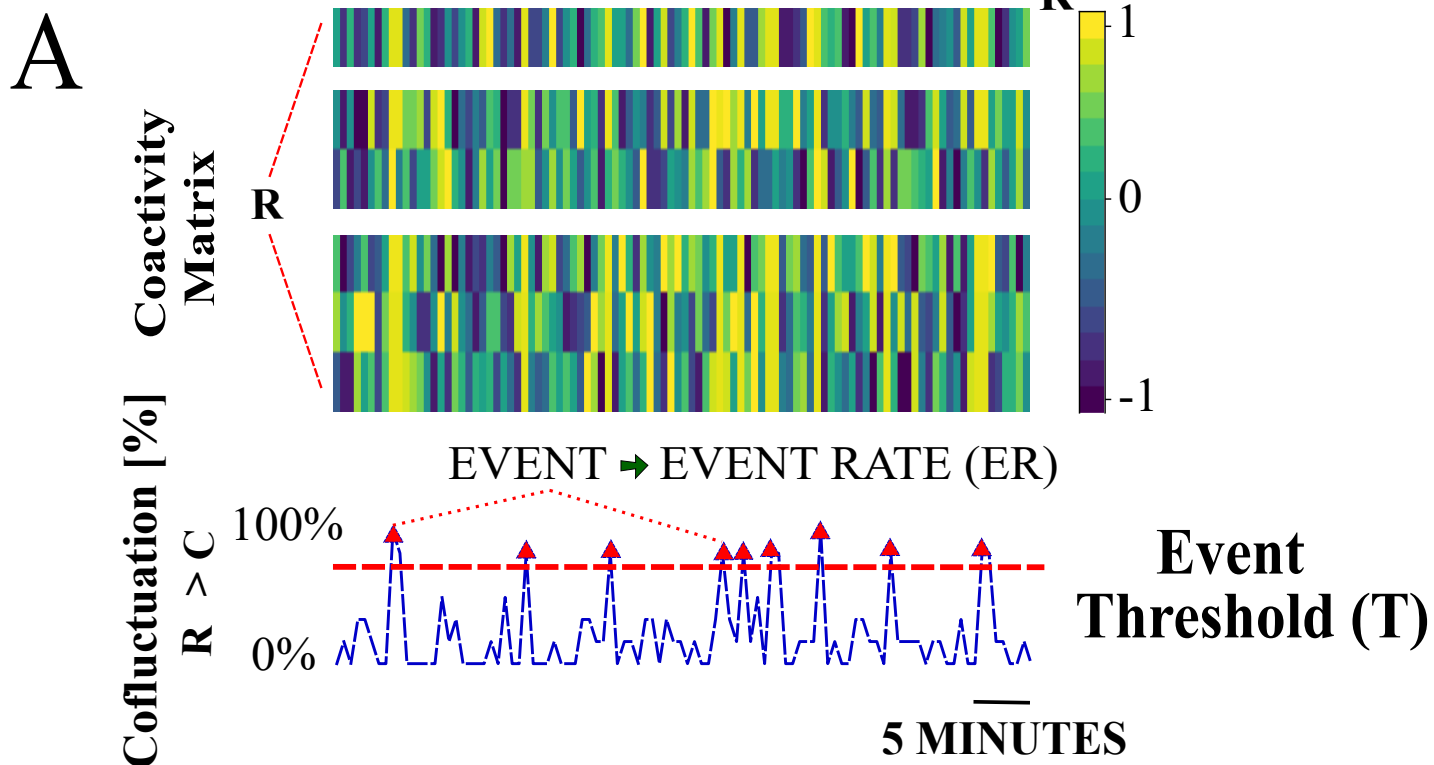


Events Computed from Spike Rate<sub>STD</sub>

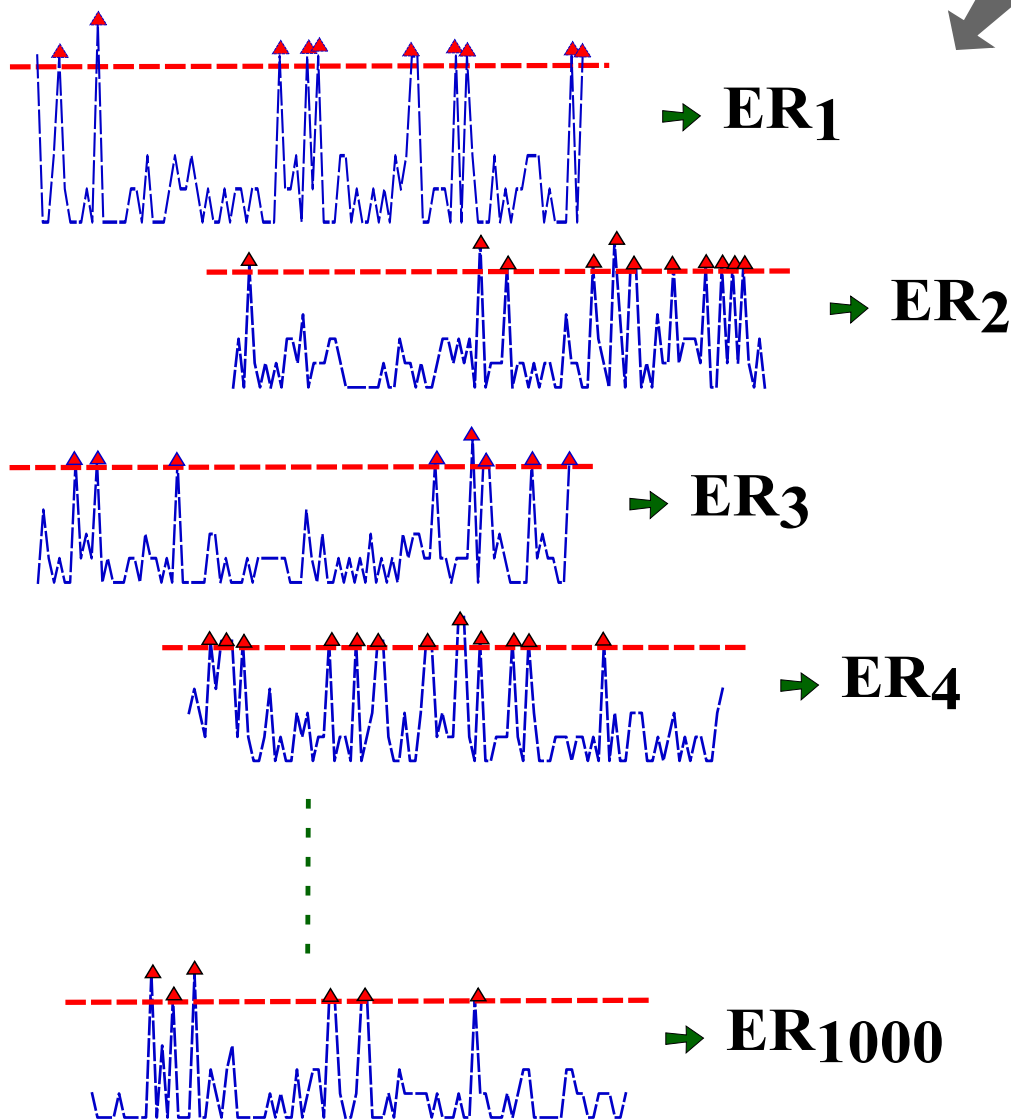






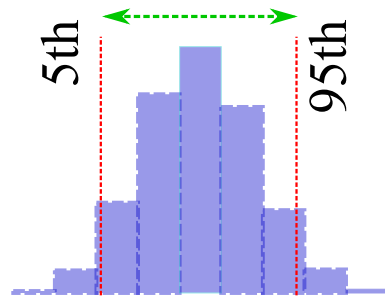


Multiple Cofluctuation (C) Time Series Bootstrapped  
1000 Times with Multiple Event Thresholds (T)



A

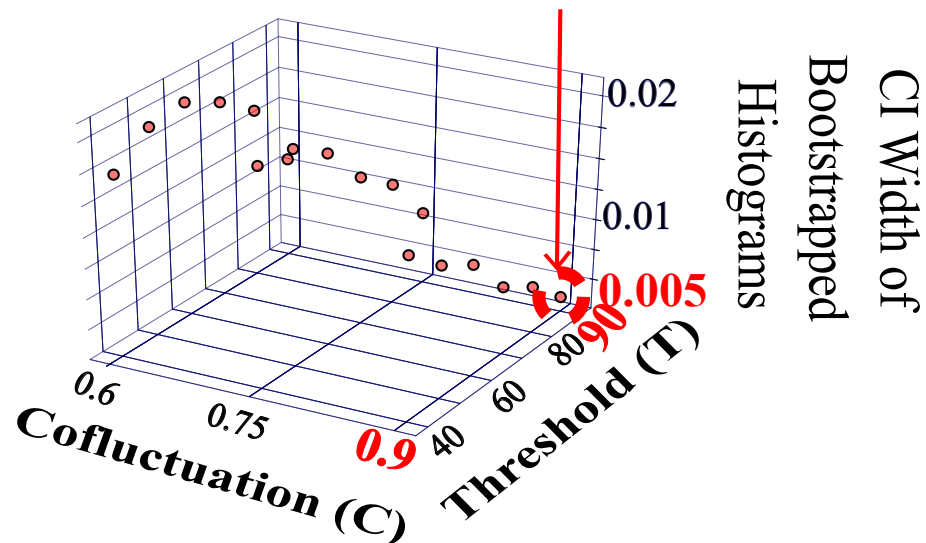
# 95% Confidence Interval (CI) Width



Bootstrapped Histogram of 1000 Events Rates (ER) for a Cofluctuation (C) & Event Threshold (T) Pair  
95% CI Widths Plotted for Different C,T Pairs for a Single Animal

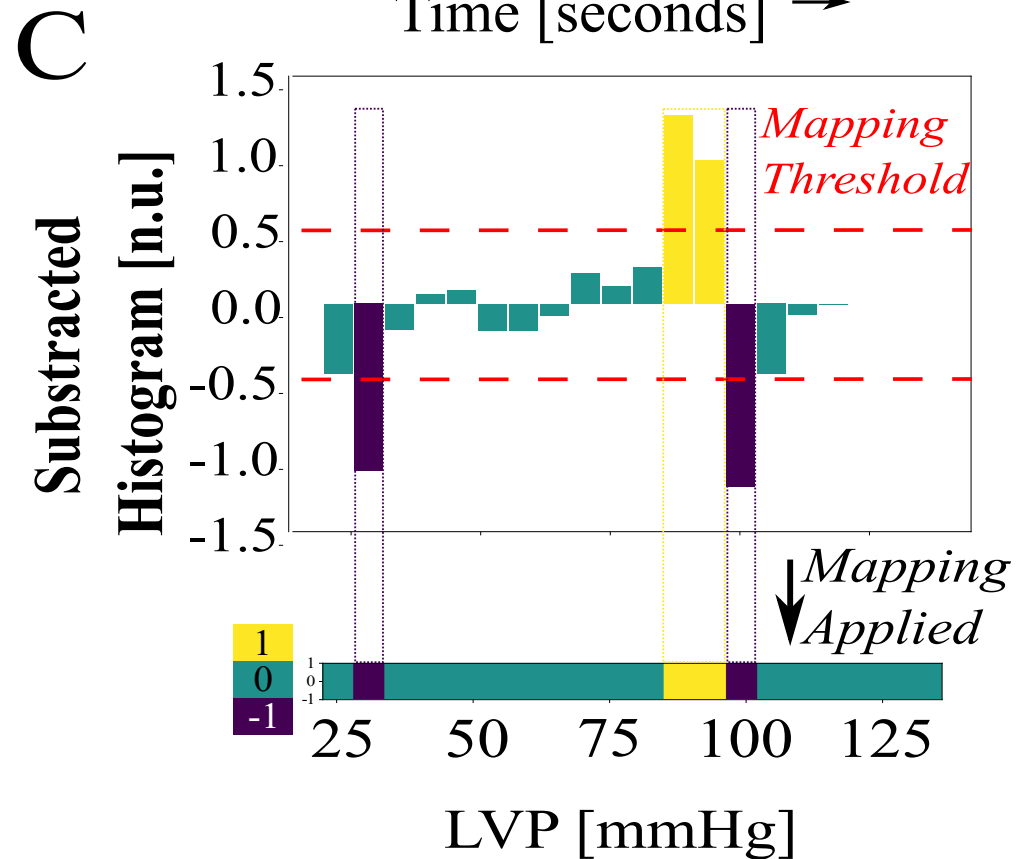
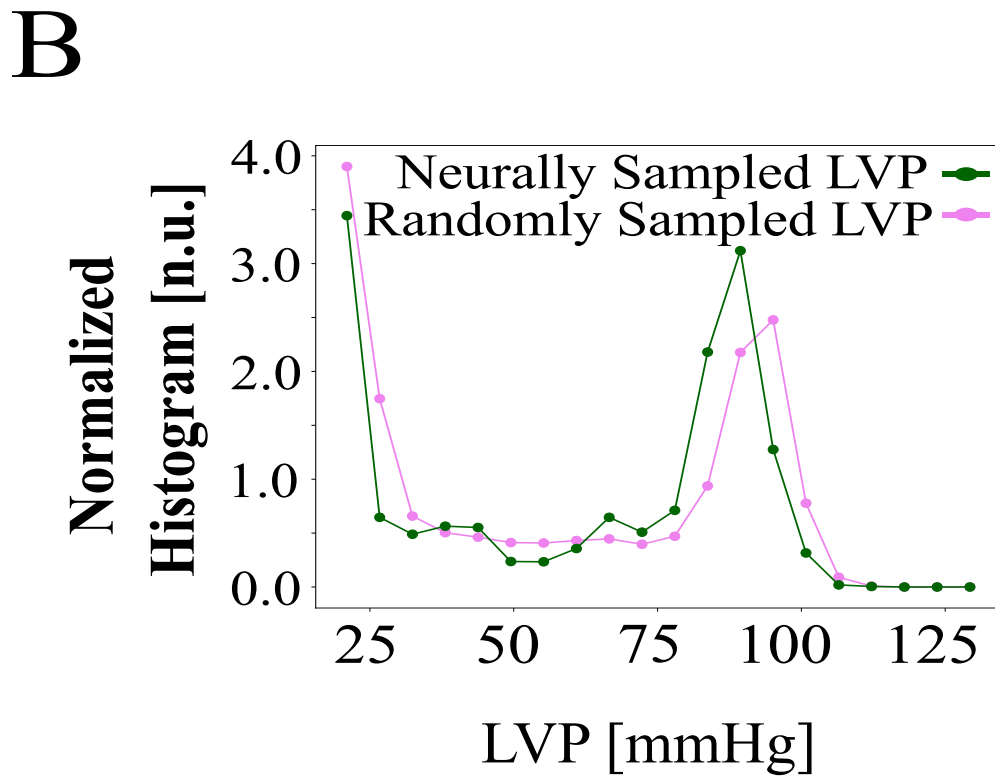
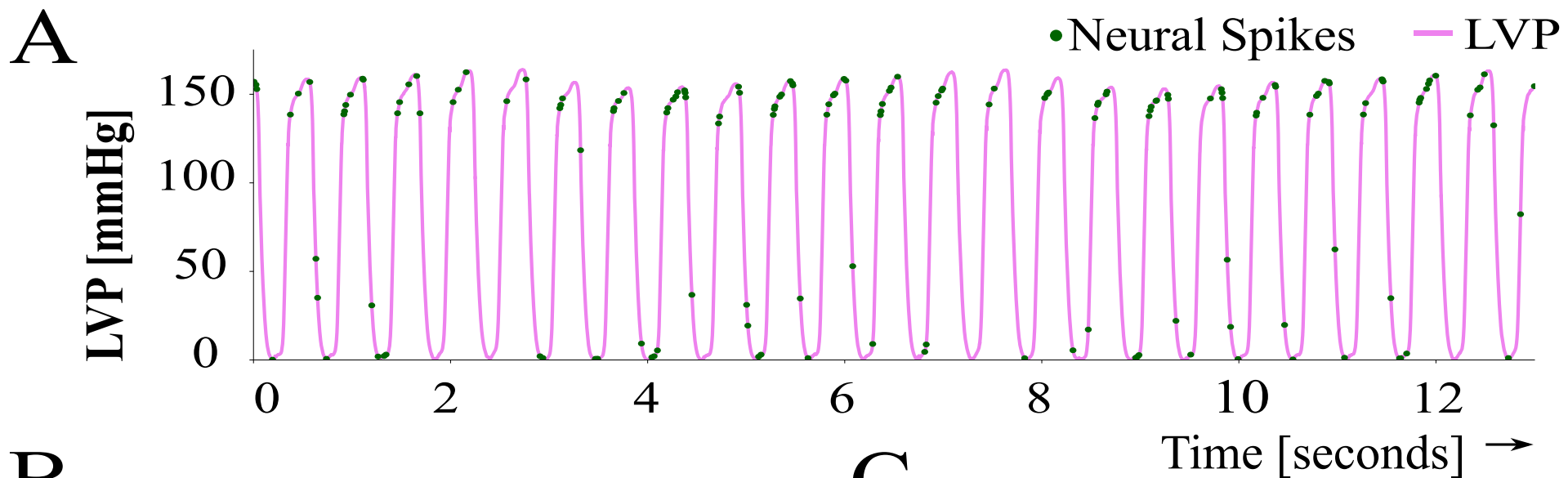
B

Individualized Optimum Cofluctuation (C) & Event Threshold (T) Pair Resulting in Minimum CI Width: **C = 0.9, T = 90**

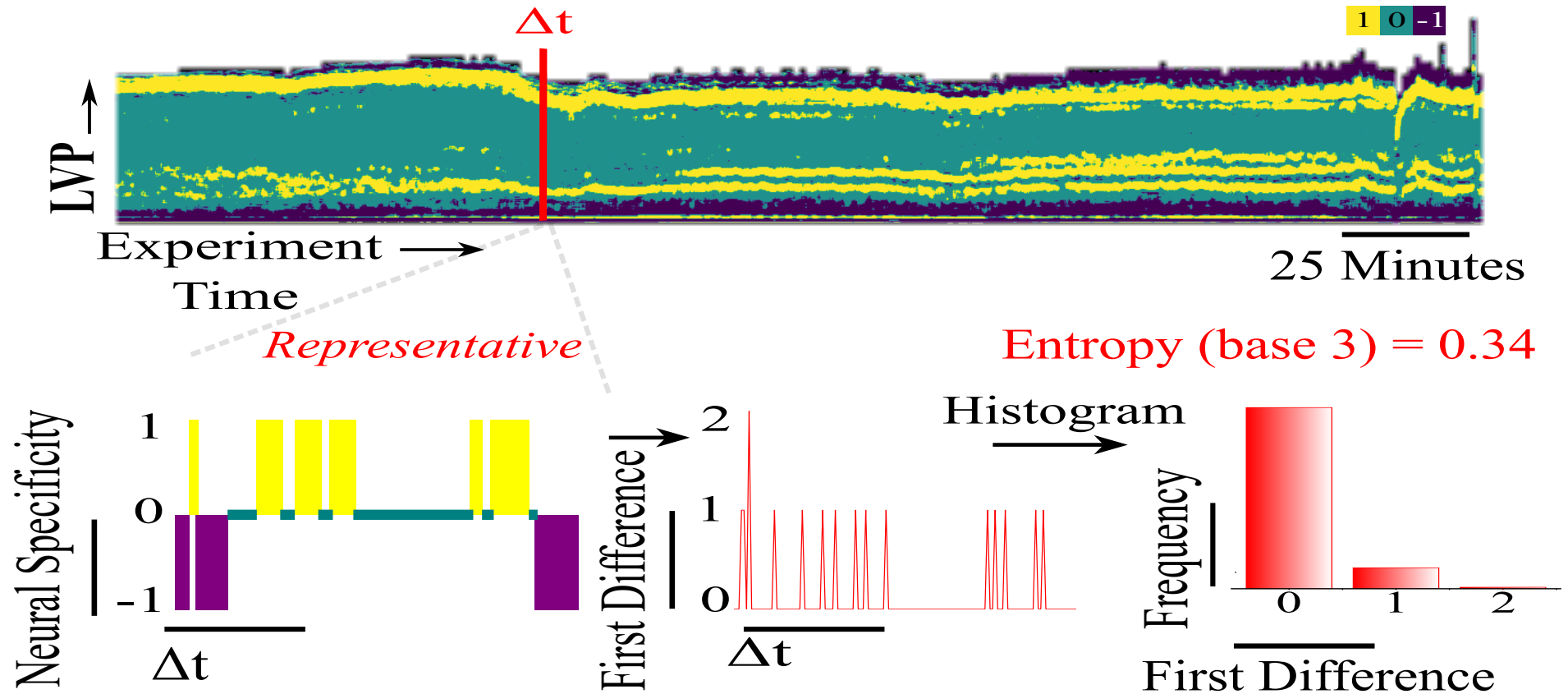


C

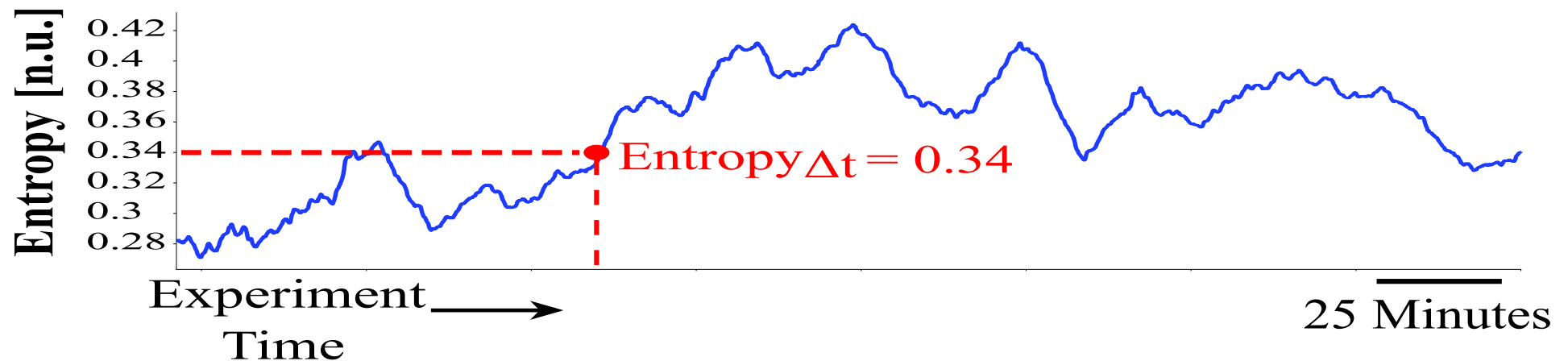
Animal#	Optimum Cofluctuation (C)	Optimum Threshold (T)	Minimum CI Width	
HEART FAILURE MODEL	1	0.9	70	0.005
	2	0.9	90	0.018
	3	0.75	90	0.003
	4	0.9	90	0.014
	5	0.9	90	0.003
	6	0.9	90	0.026
	7	0.9	90	0.011
	8	0.9	90	0.009
	9	0.9	90	0.014
	10	0.9	90	0.014
	11	0.9	90	0.004
CONTROL	1	0.9	60	0.001
	2	0.9	90	0.002
	3	0.75	90	0.004
	4	0.9	90	0.006
	5	0.9	90	0.004
	6	0.9	90	0.003



# Neural Specificity Throughout the Experiment per Channel



## B Entropy Throughout the Experiment per Channel



# Coactivity Matrix from Sliding Mean Spike Rate

